Chaotic Mixing in Three Dimensional Porous Media

Daniel R. Lester[1]†, **Marco Dentz**[2]
and Tanguy Le Borgne[3]

[1]School of Civil, Environmental and Chemical Engineering, RMIT University, 3000 Melbourne, Victoria, Australia
[2]Spanish National Research Council (IDAEA-CSIC), 08034 Barcelona, Spain
[3]Geosciences Rennes, UMR 6118, Université de Rennes 1, CNRS, 35042 Rennes, France

(?; revised ?; accepted ?. - To be entered by editorial office)

Under steady flow conditions, the topological complexity inherent to all random 3D porous media imparts complicated flow and transport dynamics. It has been established that this complexity generates persistent chaotic advection via a three-dimensional (3D) fluid mechanical analogue of the Baker's map which rapidly accelerates scalar mixing in the presence of molecular diffusion. Hence pore-scale fluid mixing is governed by the interplay between chaotic advection, molecular diffusion and the broad (power-law) distribution of fluid particle travel times which arise from the non-slip condition at pore walls. To understand and quantify mixing in 3D porous media, we consider these processes in a model 3D open porous network and develop a novel stretching continuous time random walk (CTRW) which provides analytic estimates of pore-scale mixing which compare well with direct numerical simulations. We find that chaotic advection inherent to 3D porous media imparts scalar mixing which scales exponentially with longitudinal advection, whereas the topological constraints associated with 2D porous media limits mixing to scale algebraically. These results decipher the role of wide transit time distributions and complex topologies on porous media mixing dynamics, and provide the building blocks for macroscopic models of dilution and mixing which resolve these mechanisms.

Key words: Lagrangian chaos, porous media, mixing, scalar transport

1. Introduction

All porous media, whether random or ordered, granular or networked, heterogeneous or homogeneous, are typified by the geometric and topological complexity of the pore-space (Scholz *et al.* 2012; Vogel 2002). This pore-space plays host to a wide range of fluid-borne processes including transport, mixing and dispersion, chemical reaction and microbiological activity, all of which are influenced by the flow structure and transport properties (Metcalfe *et al.* 2012; Dentz *et al.* 2011; de Barros *et al.* 2012; Chiogna *et al.* 2012). Whilst the global distribution of a concentration plume over the porous network is important, local fluid mixing at the pore-scale also plays a key role in the control of both fluid-fluid reactions (e.g. redox processes) and fluid-solid reactions (e.g. precipitation-dissolution processes), which are of importance for a range of subsurface operations, including CO_2 sequestration, contaminant remediation or geothermal dipoles

---

† Email address for correspondence: daniel.lester@rmit.edu.au

management. Although pore-scale flows are often smooth and steady (typically Stokesian or laminar), the complexity of the pore-space renders upscaling transport and mixing processes a challenging task.

Because of their fundamental role in driving chemical reactions, mixing processes have received increasing attention in recent years in the context of porous media flows (Dentz *et al.* 2011). Two-dimensional (2D) laboratory experiments (Gramling *et al.* 2002; Tartakovsky *et al.* 2008*a*; de Anna *et al.* 2014) and theoretical and modeling studies (Battiato *et al.* 2009) have shown that upscaled chemical kinetics are not captured by classical macro-dispersion theories due to incomplete mixing at the pore scale. The works by Tartakovsky *et al.* (2008*b*,*c*, 2009); Battiato *et al.* (2009) discuss the relevance of local pore-scale transport and mixing processes for global Darcy scale representations of reactive transport and advocate the use of hybrid models that facilitate the communcation between pore and Darcy scale. This points to a need for predictive theories for pore-scale concentration statistics which are couched in terms of the underlying medium properties. Lamellar mixing theories, developed in the context of turbulent flows (Villermaux & Duplat 2003; Duplat & Villermaux 2008; Duplat *et al.* 2010), have been applied and extended for the prediction of concentration statistics in 2D Darcy scale heterogeneous porous media (Le Borgne *et al.* 2013, 2015). A central element of this theory is to quantify the link between fluid stretching and mixing. In this context, linking the pore network topological properties to the local pore-scale mixing dynamics is an essential step, which we explore in this study.

In 2D steady flows, a consequence of the Poincaré-Bendixson theorem is that fluid streamlines cannot cross each other and so may only diverge or converge over finite periods. An important consequence of this topological constraint is that hyperbolic (exponential) stretching cannot persist over arbitrarily long times and the only persistent fluid deformation is via shear. This constraint is clearly uncovered by transforming the velocity gradient in such flows into streamline coordinates (Dentz *et al.* 2015). Hence fluid stretching in steady 2D flows can only scale algebraically in time, whereas in 3D steady flows much richer behaviour is possible.

Indeed, the topological complexity inherent to all 3D porous media has been shown to induce chaotic advection under steady flow conditions via a 3D fluid mechanical analogue of the Baker's map (Lester *et al.* 2013). Such chaotic Lagrangian dynamics are well-known to rapidly accelerate diffusive mixing and scalar dissipation (Ottino 1989), yet have received little attention in the context of pore-scale flow. From the perspective of advective transport, the distribution of pore sizes and shapes, together with no-slip boundary conditions at the pore walls, are known to impart non-Gaussian pore velocity distributions (Moroni & Cushman 2001; Bijeljic *et al.* 2011; Kang *et al.* 2014; Holzner *et al.* 2015), which lead to a rich array of dispersion phenomena ranging from normal to super-diffusive. The continuous time random walk (CTRW) approach (Berkowitz *et al.* 2006) has been used to model this behaviours (Bijeljic *et al.* 2003; Le Borgne *et al.* 2011; de Anna *et al.* 2013; Kang *et al.* 2014; Holzner *et al.* 2015) based on the transit time distributions over characteristic pore lengths, which reflect the distribution of pore velocities. The interplay of wide transit time distributions and chaotic advection at the pore-scale impacts both macroscopic transport and dispersion as well as pore-scale dilution.

Pore-scale chaotic advection has also been shown (Lester *et al.* 2014) to significantly suppress longitudinal dispersion arising from the no-slip wall condition due to transverse mixing generating an analogue of the Taylor-Aris mechanism. Conversely, the wide transit time distributions are expected to have a drastic impact on the dynamics of transverse mixing in conjunction with chaotic advection as the transit times set the timescales over which significant stretching of a material fluid element occurs. While the impact of broad transit time distributions on the spatial spreading of transported elements is well understood, their impact upon mixing is an open question. As shown in Lester *et al.* (2014), Lagrangian chaos generates ergodic particle trajectories at the pore-scale, and the associated decaying correlations allows the advection process to be modelled as a stochastic process. During advection through the pore-space, fluid elements undergo punctuated stretching and folding (transverse to the mean flow direction) events at pore junctions, leading to persistent chaotic advection in random porous media. Such dynamics have been captured in an idealized 3D pore network model which contains the basic features common to all porous media, namely chaotic advection and no-slip boundary conditions, and so represents the minimum complexity inherent to all porous media.

In this paper we develop a novel stretching CTRW which captures the advection and deformation of material elements through this porous network model. This CTRW model is solved analytically in conjunction with an advection-diffusion equation (ADE) for for solute concentration, and thus describes mixing under the combined action of chaotic advection, molecular diffusion and wide transit time distributions within the pore space. Analytic model predictions are verified against numerical calculations and governing parameters identified. This formalism allows prediction of concentration PDF evolution within the pore-space and quantification of the impact of chaotic advection upon mixing directly in terms of the relevant network properties.

To simplify exposition we consider the steady state pore-scale mixing of a concentration field which is heterogeneous at the pore-scale but homogeneous at the macro-scale, and these results are then extended to describe pore-scale mixing for an arbitrary macroscopic concentration distribution. We compare predictions of pore-scale mixing between random 3D porous networks which admit Lagrangian chaos and 2D networks which only permit non-chaotic dynamics. Hence we quantify the impact of both network topology and structure upon pore-scale mixing and dispersion. These results form a quantitative basis for upscaling of pore-scale dynamics to macroscopic mixing and transport models, and establish the impacts of ubiquitous chaotic mixing in 3D random porous media.

The paper is organized as follows; the mechanics of chaotic mixing in 3D porous media are briefly reviewed in § 2, followed by a description of the 3D open porous network model in § 3. Fluid stretching in this model network is discussed in § 4, from which a stretching CTRW model is derived in § 5. This model is then used to quantify mixing in § 6, and evolution of the concentration PDF, mixing scale and dispersion are considered in § 7 and conclusions are made in § 8.

2. Pore-Scale Chaotic Advection in 3D Porous Media

In this Section we summarise the mechanisms which generate pore-scale chaotic advection as described in (Lester *et al.* 2013), and further explain the role of critical points of the skin friction field. Topological complexity is a defining feature of all porous media - from granular and packed media to fractured and open networks - these materials are all typified by a highly connected pore-space. Such topological complexity is characterised by the Euler characteristic χ (related to the topological genus g as $\chi = 2(1-g)$) which measures the connectivity of the pore-space (Vogel 2002) as

$$\chi = N - C + H, \tag{2.1}$$

where N is the number of pores, C the number of redundant connections and H the number of completely enclosed cavities. For porous media it is more meaningful to consider the average number density of these quantities, where from computer tomography studies (Vogel 2002) it is found that typically N is large whilst C, H are small. Hence

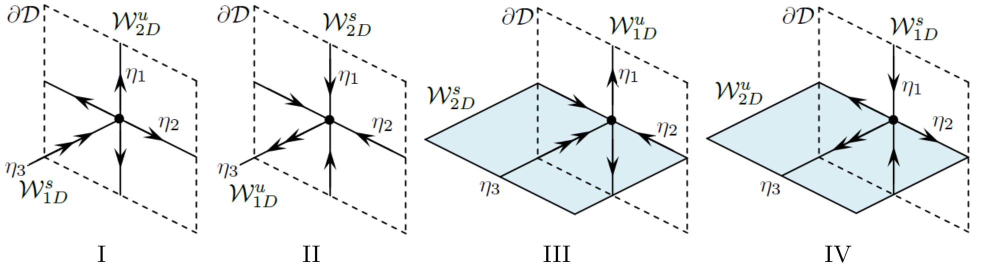

FIGURE 1. Schematic of type I-IV critical points of the skin friction field $\mathbf{u}$ on the boundary $\partial\mathcal{D}$ and associated stable and unstable manifolds $\mathcal{W}^s$, $\mathcal{W}^u$. The double arrows reflect the eigenvalue sum $\eta_1+\eta_2+2\eta_3=0$ in (2.5).

the number density of the Euler characteristic χ is typically large and negative (Scholz *et al.* 2012; Vogel 2002), reflecting topologically complex media.

When a continuous fluid is advected through such media, a large number of critical points (zeros) $\mathbf{x}_p$ arise in the skin friction field $\mathbf{u}(\mathbf{x})$ at the boundary $\partial\mathcal{D}$ of the fluid domain $\mathcal{D}$. The skin friction field $\mathbf{u}(\mathbf{x})$ is defined as

$$\mathbf{u}(\mathbf{x})=\mathbf{u}(x_1,x_2,x_3):=\frac{\partial\mathbf{v}}{\partial x_3}, \tag{2.2}$$

where $\mathbf{v}(x_1,x_2,x_3)$ is the velocity field, x_3 the coordinate normal to the fluid boundary $\partial\mathcal{D}$ and the x_1, x_2 coordinates are tangent to this boundary (Surana *et al.* 2006; de Winkel & Bakker 1988; Chong *et al.* 2012). The critical points $\mathbf{x}_p$ of the skin friction field $\mathbf{u}$, (where $\mathbf{u}(\mathbf{x}_p)=\mathbf{0}$) represent the boundary counterpart to stagnation points $\mathbf{x}_0$ of the interior flow field $\mathbf{v}$ (where $\mathbf{v}(\mathbf{x}_0)=\mathbf{0}$). Note that stagnation points do not arise under pressure-driven Stokes flow as no mechanism exists to generate flow reversal.

The Poincaré-Hopf theorem states that the sum of the indices γ_p of critical points $\mathbf{x}_p$ is related to the topological genus g and Euler characteristic χ as

$$\sum_p \gamma_p(\mathbf{x}_p)=2(1-g)=\chi, \tag{2.3}$$

where the index $\gamma_p=-1$ for saddle points, $\gamma_p=1$ for node points and $\gamma_p=0$ for centers of the skin-friction field. Hence $|\chi|$ represents a lower bound for the number density of saddle points under steady 3D Stokes flow, which as shall be shown, impart significant fluid stretching into the fluid interior. A relevant question is what is the impact of this stretching with respect to advection in porous media?

Critical points play an important role with respect to the Lagrangian dynamics of 3D steady flows, as it is at these points that the formal analogy between transport in steady 3D volume-preserving flows and 1 degree-of-freedom Hamiltonian systems breaks down (Bajer & Moffatt 1990; Bajer 1994), and such points are widely (Mezić & Wiggins 1994; Wiggins 2010) implicated in the creation of Lagrangian chaos. Associated with these critical points are stable $\mathcal{W}^s$ and unstable $\mathcal{W}^u$ manifolds which project into the fluid interior, and these may be either 1D or 2D as shown in Figure 1. MacKay (1994, 2008) proposes that the manifolds which are 2D represent surfaces of minimal transverse flux, and so the set of these co-dimension 1 manifolds form the “skeleton” of the flow which organize transport and mixing throughout the fluid domain. Whilst 1D manifolds also play a role, they are less important as they do not separate the fluid domain.

The dimensionality of these interior manifolds $\mathcal{W}^s$, $\mathcal{W}^u$ is dictated by the type of critical point (saddle, node, centre) and hence the index γ. Fluid deformation local to critical points $\mathbf{x}_p$ is quantified by the linearized skin friction tensor $\mathcal{A}=\partial\mathbf{u}/\partial\mathbf{x}|_{\mathbf{x}_p}$ which is the boundary counterpart of the strain-rate tensor $\mathcal{F} = \partial\mathbf{v}/\partial\mathbf{x}|_{\mathbf{x}_0}$ which quantifies deformation local to the stagnation points $\mathbf{x}_0$. The components a_{ij} of the skin friction tensor $\mathcal{A}$ are given by the expansion

$$u_i = \sum_{j=1}^{3} a_{ij}(x_j - x_{p,j}) + \mathcal{O}((x_j - x_{p,j})^2), \tag{2.4}$$

and de Winkel & Bakker (1988); Chong *et al.* (2012) have derived the normal form of $\mathcal{A}$ around a critical point $\mathbf{x}_p$ in an incompressible flow as

$$\mathcal{A} = \begin{pmatrix} a_{11} & a_{12} & a_{13} \\ a_{21} & a_{22} & a_{23} \\ 0 & 0 & -\frac{1}{2}(a_{11} + a_{22}) \end{pmatrix}. \tag{2.5}$$

For incompressible flow the eigenvalues ν_i of $\mathcal{F}$ satisfy $\sum_{i=1}^{3} \nu_i = \nabla \cdot \mathbf{v} = 0$, whereas the eigenvalues η_i of $\mathcal{A}$ satisfy $\sum_{i=1}^{3} \eta_i = \nabla \cdot \mathbf{u} = -\eta_3$, where η_1, η_2 are the eigenvalues in the skin friction boundary (with $\eta_1 \leqslant \eta_2$), and η_3 the interior eigenvalue. Hence critical points consist of one stable and two unstable eigenvalues or vice-versa, and $\eta_3 > 0$ for separation points and $\eta_3 < 0$ for reattachment points. As (2.5) indicates that the boundary $\partial\mathcal{D}$ is invariant, there exist four critical point types as shown in Figure 1:

- Type I separation point $\eta_3 > 0$, attractor for $\mathbf{u}$ with $\eta_1, \eta_2 < 0$,
- Type II reattachment point $\eta_3 < 0$, repeller for $\mathbf{u}$ with $\eta_1, \eta_2 > 0$,
- Type III separation point $\eta_3 > 0$, saddle for $\mathbf{u}$ with $\eta_1 < 0$, $\eta_2 > 0$,
- Type IV reattachment point $\eta_3 < 0$, saddle for $\mathbf{u}$ with $\eta_1 < 0$, $\eta_2 > 0$.

Type I, II are node points, whilst type III, IV are saddle points and so the associated interior manifolds are 2D, forming barriers to transport in the fluid interior. Figure 2 illustrates these features for pore branch (a) and merge (b) elements (the union of which is termed a couplet) in an open porous network. Here, the saddle-type reattachment (type IV) and separation point (type III) points arise due to the basic topology of the pore branch and merger, and these generate the respective interior 2D manifolds $\mathcal{W}^u_{2D}$, $\mathcal{W}^s_{2D}$. Whilst the geometry of pore branches and mergers may vary significantly, the basic topology shown in Figure 2 is universal to almost all pore branches and mergers.

The interaction of the 2D interior manifolds $(\mathcal{W}^s_{2D}, \mathcal{W}^u_{2D})$ control fluid transport and mixing. If these 2D manifolds intersect transversely a heteroclinic tangle and chaotic dynamics results, whereas a smooth heteroclinic connection between yields a 2D stream-surface that acts as a separatrix between saddle points. For the pore junction shown in Figure 2, significant fluid stretching occurs transverse to the 2D interior manifolds, and folding of material elements arises from advection over the critical points $\mathbf{x}_p$. These stretching and folding actions are the constituent motions of the Smale horsehoe map, a hallmark of chaotic dynamics in continuous systems. If a connected pore branch and merger are oriented symmetrically (as reflected by zero offset angle θ in Figure 2), then this symmetry results in a smooth heteroclinic connection between the 2D manifolds. Conversely, when these pore elements are oriented with non-zero offset angle $\theta \neq 0$, this symmetry is broken, resulting in transverse heteroclinic intersection of the 2D manifolds and hence chaotic streamline dynamics. The disordered nature of random porous media ensures that $\theta \neq 0$ and these symmetries are broken, leading to chaotic advection under steady flow conditions. Whilst porous media may exhibit other features such as surface roughness or pore tortuosity which may also generate chaotic advection (Jones *et al.* 1989; Ottino & Wiggins 2004), a large density of saddle-type critical points is generic to

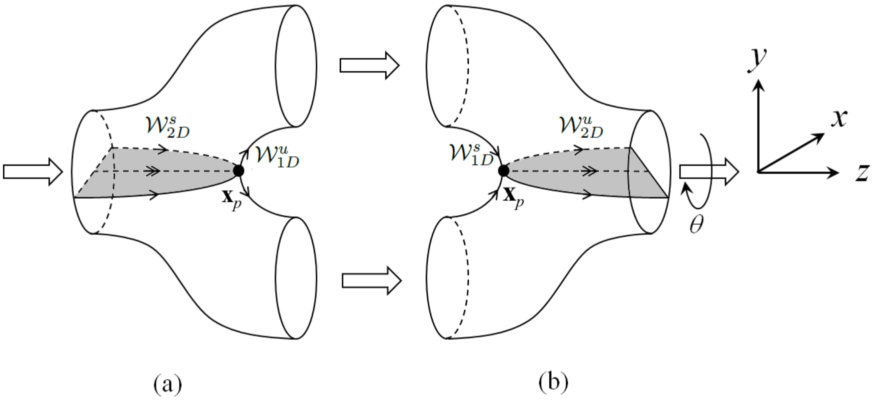

(a) (b)

Figure 2. Schematic of pore branch (a) and merge (b) elements, where black dots shows the critical separation and attachment points respectively and grey surfaces denote the associated 2D stable and unstable manifolds representing 2D surfaces of locally minimum transverse flux, the "skeleton" of the flow. The angle θ denotes the relative orientation of the pore branch and merger elements.

all complex media, hence the mechanisms described above represents a lower bound for chaotic dynamics inherent to porous media flow.

3. 3D Open Porous Network Model

To study the impacts of such topology-induced chaotic advection upon transport and mixing in porous media, we consider a model 3D open porous network which consists of random network of connected pore junctions and mergers shown in Figure 2. This model is briefly summarised here, further details can be found in (Lester *et al.* 2016). We consider a 3D random network of these pore branches and mergers which is the simplest representation of a topologically complex open porous network which is homogeneous at the macroscale. Due to the spatial symmetries and reversibility of Stokes flow in these elements, we shall use a series of linear spatial transformations (reflection, scaling, reorientation, inversion) to map fluid transport and deformation in Stokes flow in the elements in Figure 2 to construct the entire network. In this way we can develop a highly efficient model of fluid transport and deformation over a random 3D network.

To compose a 3D network over the semi-infinite domain $\Omega : \mathbf{x} \in \mathbb{R}^3, z > 0$, we use the pore branch and merge elements shown in Figure 2 to connect a series of so-called "mapping planes" oriented parallel to the (x, y) plane, distributed along the z-axis at integer multiples of the pore element length ℓ. Each mapping plane consists of an infinite number of reflections in the x, y directions of a periodic square $(x, y) \in [0, L] \times [0, L]$ which contains $3J$ randomly-located non-overlapping pores, as shown in Figure 3. The location of the j-th pore in the n-th mapping plane is labelled $\mathbf{r}_{n,j} = (x_{n,j}, y_{n,j}, n\ell)$. Of these $3J$ pores, J are randomly labelled as "branch" pores (i.e. pores which branch next in the positive z direction), and the remaining $2J$ pores are labelled as "merge pores" (i.e. those which are about to merge). A branch pore at plane n is connected to two merge pores at plane $n + 1$ by a pore branch element located between these planes, and conversely two branch pores at plane n are connected with a single merge pore at plane n by a pore merge element as per Figure 2.

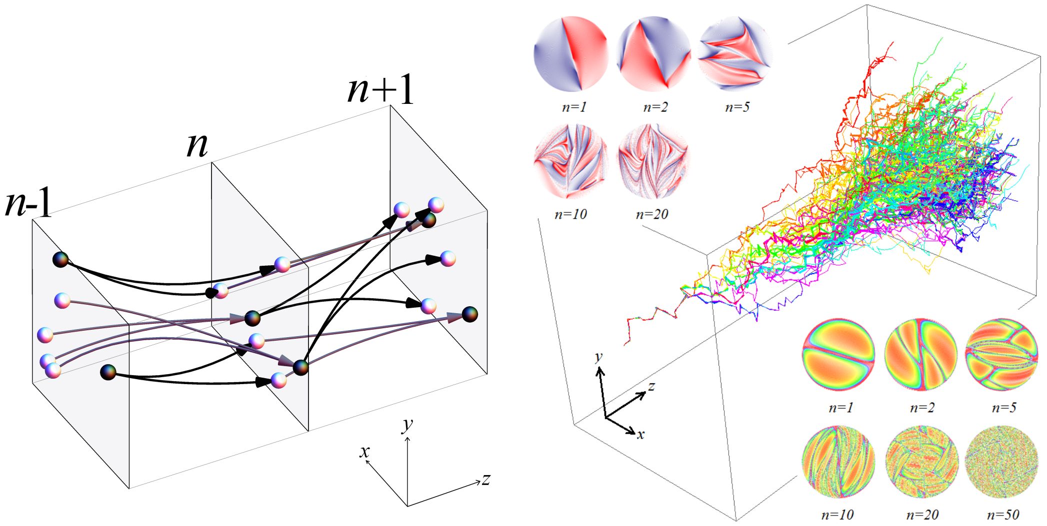

(a) (b)

FIGURE 3. (a) Schematic of pore branches (black) and mergers (white) between mapping planes, with branch pores (black) and merge pores (white) shown. (b) (middle) Evolution of 10^5 non-diffusive particles in the pore network from continuous injection in a single pore, (upper left) typical transverse distribution of non-diffusive coloured fluid particles with longitudinal pore number n, (lower right) typical distribution of residence times (pink = maximum, orange=minimum) with longitudinal pore number n.

To accommodate connections between the merge pore locations $\mathbf{r}_{m_1}, \mathbf{r}_{m_2}$ and the branch pore location $\mathbf{r}_{b_1}$ at adjacent mapping planes, the pore branch and merge elements are rotated and stretched such that the $\hat{\mathbf{e}}_y$, $\hat{\mathbf{e}}_z$ vectors are aligned along $\mathbf{r}_{m_1} - \mathbf{r}_{m_2}$, $\mathbf{r}_{b_1} - \frac{1}{2}(\mathbf{r}_{m_1} + \mathbf{r}_{m_2})$ respectively, and the element height and length are re-scaled to $||\mathbf{r}_{m_1} - \mathbf{r}_{m_2}||$, $||\mathbf{r}_{b_1} - \frac{1}{2}(\mathbf{r}_{m_1} + \mathbf{r}_{m_2})||$ respectively. The orientation angle φ in the (x, y) plane of a pore branch/merge element is then

$$\varphi = \arctan\left(\frac{(\mathbf{r}_{m_1} - \mathbf{r}_{m_2}) \cdot \hat{\mathbf{e}}_y}{(\mathbf{r}_{m_1} - \mathbf{r}_{m_2}) \cdot \hat{\mathbf{e}}_x}\right), \tag{3.1}$$

and the relative angle θ between subsequent elements is defined as $\theta_n = \varphi_{n+1} - \varphi_n$. Hence the set of non-overlapping pore locations $\mathbf{r}_{n,j}$ for $n = 0 : \infty$, $j = 1 : 3J$ completely defines a realization of the 3D open porous network, and the ensemble of all realizations of the porous network is ergodic and stationary. The resultant random orientation angle φ is uniformly distributed and is uncorrelated both across and within mapping planes, hence transport within the 3D open porous network may be described by a Markov process in space.

To model transport within the porous network, we solve the fluid velocity field $\mathbf{v}$ for Stokes flow $\mu\nabla^2\mathbf{v} + \nabla p = 0$ within the pore branch element Ω driven by a differential pressure $p|_{z=0} - p|_{z=L} = \Delta p$, subject to the no-slip boundary condition $\mathbf{v}|_{\partial\Omega} = 0$. The flow field is calculated numerically to order 10^{-16} RMS accuracy using the finite-volume CFD package ANSYS-CFX with double precision calculation. The advection dynamics for passive tracer particles within the branch element Ω under Stokes flow can be represented by the spatial $\mathcal{M}^*$ and temporal $\mathcal{T}^*$ maps

$$\mathcal{M}^* : \{x_{r,n}, y_{r,n}\} \mapsto \{x_{r,n+1}, y_{r,n+1}\}, \tag{3.2}$$

$$\mathcal{T}^* : t_n \mapsto t_{n+1} \tag{3.3}$$

where $\{x_{r,n}, y_{r,n}\}$ are the x, y particle positions relative to the inlet of Ω (where $x_{r,n}^2 + y_{r,n}^2 = 0, 1$ correspond to the pore centre and boundary respectively), and $\{x_{r,n+1}, y_{r,n+1}\}$ are the positions relative to the outlet of Ω. Note that $x_{r,n+1}, y_{r,n+1}$ do not reflect the specific outlet pore the particle travels to, as a direct consequence of the reflection symmetry of the flow about the plane $y_r = 0$. Similarly, the temporal map $\mathcal{T}^*$ describes the residence time from the inlet to outlet planes. From the CFD results, the exact spatial $\mathcal{M}^*$ and temporal $\mathcal{T}^*$ maps are remarkably well approximated (within error $\epsilon \sim 10^{-3}$) by composites of the following simple analytic maps

$$\mathcal{M} : \{x_r, y_r\} \mapsto \begin{cases} \{x_r, 2y_r - \sqrt{1 - x_r^2}\} & \text{if} \quad y_r > 0 \\ \{x_r, 2y_r + \sqrt{1 - x_r^2}\} & \text{if} \quad y_r \leqslant 0 \end{cases}, \tag{3.4}$$

$$\mathcal{T} : t \mapsto t + \frac{1}{1 - x_r^2 - y_r^2}, \tag{3.5}$$

where for a pore branch $\mathcal{M}^* \approx \mathcal{M}$, $\mathcal{T}^* \approx \mathcal{T} \circ \mathcal{M}$, and due to the reflection symmetry of Stokes flow $\mathcal{M}^* \approx \mathcal{M}^{-1}$, $\mathcal{T}^* \approx \mathcal{T} \circ \mathcal{M}^{-1}$ for a pore merger. These approximate maps greatly simplify description of the advection dynamics and preserve the essential features of advective transport, namely stretching in a pore branch (and contraction in a pore merger) of fluid elements by a factor of 2 in the y-direction, and the Poiseuille-like distribution of $\mathcal{T}$ (scaled such that the minimum advection time is unity) due to the no-slip boundary conditions. The composite $\mathcal{T}^* \approx \mathcal{T} \circ \mathcal{M}$ accurately captures the residence time distribution because the advection map $\mathcal{M}$ accurately captures the streamline geometry, and the no-slip boundary condition within Ω dominates temporal advection,hence a simple Poiseuille distribution concatenated with $\mathcal{M}$ accurately approximates the temporal map $\mathcal{T}^*$. Whilst the advective maps $\mathcal{M}$, $\mathcal{M}^{-1}$ are not area-preserving, they are implicitly volume-preserving when deformation in the z-direction is considered

Whilst the symmetry of the pore branch and merger results in zero fluid stretching (as reflected by the concatenation $\mathcal{M}^{-1} \circ \mathcal{M} = I$, where I is the identity operator), these elements at arbitrary orientations in the xy-plane can break this symmetry and lead to persistent fluid stretching. The reoriented advective maps $\mathcal{S}(\varphi)$, $\mathcal{S}^{-1}(\varphi)$ define transport in pore branches and mergers at arbitrary angles

$$\mathcal{S}(\varphi) = R(\varphi) \circ \mathcal{M} \circ R(-\varphi), \qquad \mathcal{S}^{-1}(\varphi) = R(\varphi) \circ \mathcal{M}^{-1} \circ R(-\varphi), \tag{3.6}$$

where $R(\varphi)$ is a rotation operator and $\mathcal{S}^{-1}(\varphi_{n+1}) \circ \mathcal{S}(\varphi_n) \neq I$ for $\theta_n = \varphi_{n+1} - \varphi_n \neq 0$. Coupled with the residence time distribution $\mathcal{T}$, the composite maps $\mathcal{S}$, $\mathcal{S}^{-1}$ quantify advective transport relative to a local co-moving reference frame through the 3D porous network, and so the position and residence time of fluid particles can be rapidly propagated via these approximate maps, as shown in Figure 3 . Hence the sequence of alignment angles $\varphi_1, \varphi_2, \ldots$ for a particular trajectory can impart either regular or chaotic advection at the pore-scale (Lester *et al.* 2013), and the associated infinite-time Lyapunov exponent for ordered porous media spans $\lambda_\infty \in [0, \ln 2]$. Conversely, for random media θ_n is uniformly distributed over $[-\pi, \pi]$ and so always generates chaotic advection.

This basic pore network model has been used (Lester *et al.* 2013, 2014, 2016) to study the impact of pore-scale chaotic advection upon dispersion in porous media, i.e. the spatial spreading of transport particles. Figure 3 (b) illustrates the evolution of 10^5 non-diffusive particles propagated by the composite maps $\mathcal{S}$, $\mathcal{S}^{-1}$ through a realization of the random network. The lower right sub-figure in Figure 3 (b) illustrates the creation of fine-scale structure via chaotic advection within the pore-scale (from an initially segregated distribution of half blue/half red points across all pores), and the upper left subfigure shows evolution of the residence time distribution evolved via the composite temporal maps $\mathcal{S} \circ \mathcal{T}$, $\mathcal{S}^{-1} \circ \mathcal{T}$. Note there is no visual evidence of folding of fluid elements in the xy-plane as folding occurs around critical points $\mathbf{x}_p$ as fluid elements are advected downstream in the z-direction.

4. Fluid Advection and Deformation in 3D Porous Networks

4.1. *Fluid Deformation in 3D Ordered Networks*

To calculate mixing within the 3D network model, we consider the deformation of a 2D material surface arising from continuous injection of 1D line at the inlet plane due the mean flow in the z-direction. It shall prove convenient to consider this steady 2D filament as an evolving 1D material line at the intersection of each mapping-plane, the constituent points of which are advected via the maps $\mathcal{S}$, $\mathcal{S}^{-1}$. Whilst fluid deformation does occur in the z-direction, the impact upon mixing is considered negligible due to close alignment of the continuously injected 2D filament with the mean flow direction. Hence the gross impact of chaotic advection upon mixing is to accelerate mixing in the xy-plane transverse to the mean flow direction z.

As the advective map $\mathcal{M}$ maps fluid particles from the inlet to outlet pores, the 2D fluid deformation gradient tensor $\mathbf{F}_{\text{2D}}$ over a pore branch is given by the Jacobian of $\mathcal{M}$ which may be linearised as

$$\mathbf{F}_{\text{2D}} = \frac{\partial \mathcal{M}_i}{\partial x_j} = \begin{pmatrix} 1 & \pm\frac{x}{\sqrt{1-x^2}} \\ 0 & 2 \end{pmatrix} \approx \begin{pmatrix} 1 & 0 \\ 0 & 2 \end{pmatrix}, \tag{4.1}$$

and likewise fluid deformation for $\mathcal{M}^{-1}$ over a pore merger is given by $\mathbf{F}_{\text{2D}}^{-1}$. The CFD results show that this linearisation well approximates fluid deformation in the pore branch and merger. The pore branch acts to stretch fluid elements by 2 in the y-direction, and contract elements by $\frac{1}{2}$ in the z-direction (not reflected in $\mathbf{F}_{\text{2D}}$), whilst the pore merger contracts elements by $\frac{1}{2}$ in the y-direction and stretches by a factor of 2 in the z-direction. To account for arbitrary orientations we consider the reoriented deformation tensors

$$\mathbf{S}_s = \mathbf{R}(\varphi_s) \cdot \mathbf{F}_{\text{2D}} \cdot \mathbf{R}^{-1}(\varphi_s), \qquad \mathbf{S}_c = \mathbf{R}(\varphi_c) \cdot \mathbf{F}_{\text{2D}}^{-1} \cdot \mathbf{R}^{-1}(\varphi_c), \tag{4.2}$$

where $\mathbf{R}(\varphi)$ is the rotation matrix, and the subscripts s and c indicate fluid stretching (in the pore branch) and compression (in the pore merger) respectively. Fluid deformation over a coupled pore branch/merge element (couplet) is then

$$\begin{aligned} \mathbf{S} := \mathbf{S}_c \cdot \mathbf{S}_s &= \mathbf{R}(\varphi_c) \cdot \mathbf{F}_{\text{2D}} \cdot \mathbf{R}(\Delta) \cdot \mathbf{F}_{\text{2D}}^{-1} \cdot \mathbf{R}^{-1}(\Delta) \cdot \mathbf{R}^{-1}(\varphi_c) \\ &= \mathbf{R}(\varphi_c) \cdot \mathbf{D}(\Delta) \cdot \mathbf{R}^{-1}(\varphi_c), \end{aligned} \tag{4.3}$$

where $\Delta = \varphi_c - \varphi_s$. Net deformation over a series of n concatenated couplets is then given by the series

$$\begin{aligned} \mathbf{\Lambda}_n &= \mathbf{R}(\varphi_n) \cdot \mathbf{D}(\Delta_n) \cdot \mathbf{R}^{-1}(\varphi_n) \cdot \dots \cdot \mathbf{R}(\varphi_1) \cdot \mathbf{D}(\Delta_1) \cdot \mathbf{R}^{-1}(\varphi_1), \\ &= \mathbf{R}(\varphi_n) \cdot \left(\prod_{j=1}^{n} \mathbf{L}(\delta_j, \Delta_j) \right) \cdot \mathbf{R}^{-1}(\varphi_n), \end{aligned} \tag{4.4}$$

where $\mathbf{L}(\delta, \Delta) := \mathbf{R}(\delta) \cdot \mathbf{D}(\Delta)$, $\delta_j = \varphi_{j+1} - \varphi_j$ for $j = 1 : n-1$ and $\delta_n = \varphi_1 - \varphi_n$. Hence

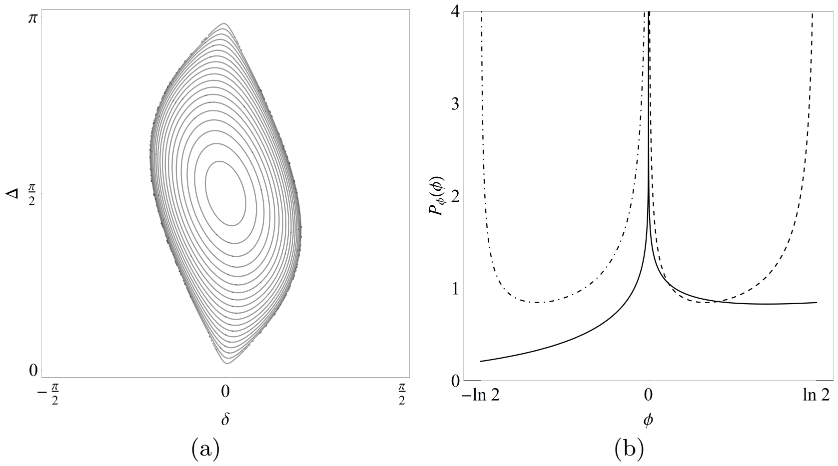

(a) (b)

FIGURE 4. (a) Contour plot of the distribution of logarithmic stretching rates $\lambda(\delta, \Delta)$ in ordered 3D networks as a function of the orientation angles δ, Δ, between and within pore couplets. The stretching rate λ varies between $\lambda = 0$ for $|\zeta| \leqslant 1$ and the theoretical maximum for continuous systems $\lambda = \ln 2$ for $\zeta = \frac{5}{4}$ at $\Delta = \pi/2$, $\delta = 0$. (b) PDF of logarithmic stretching rates $P_\phi(\phi)$ (solid), $P_{\phi_s}(\phi_s)$ (dashed) and $P_{\phi_c}(\phi_c)$ (dot-dashed) in random 3D networks. Note $P_\phi(\phi)$ is strongly peaked but asymmetric around $\phi = 0$.

the deformation tensor $\mathbf{L}(\delta, \Delta)$ quantifies fluid deformation over a series of connected pore couplets. For ordered media with fixed δ, Δ, fluid deformation is quantified by the infinite-time Lyapunov exponent λ given by the logarithm of the eigenvalues of the deformation tensor $\mathbf{L}(\delta, \Delta)$

$$\lambda(\delta, \Delta) = \pm \ln |\zeta + \sqrt{\zeta^2 - 1}|, \tag{4.5}$$

where $\zeta = \frac{9}{8}\cos\delta - \frac{1}{8}\cos(2\Delta + \delta)$. As shown in Figure 4 (a), zero net deformation occurs for $|\zeta| \leqslant 1$, whilst maximum deformation ($\lambda = \ln 2$) occurs for $\Delta = (n + \frac{1}{2})\pi$, $\delta = n\pi$, $n = 0, 1, 2, \ldots$. Hence ordered 3D porous networks represent extreme cases with respect to fluid stretching; whilst a large class ($|\zeta| \leqslant 1$) of ordered media do not exhibit chaotic advection ($\lambda = 0$), certain networks exhibit the maximum theoretic stretching ($\lambda = \ln 2$) for continuous systems.

The stretching rate $\lambda(\delta, \Delta)$ quantifies stretching of the 2D material filament as it propagates through the 3D network in the that the length l of the filament cross section in the xy-plane grows with longitudinal pore number n or distance z as

$$l(z) = l_0 \exp(\lambda(\delta, \Delta) n) = l_0 \exp\left(\lambda(\delta, \Delta)\frac{z}{\ell}\right), \tag{4.6}$$

where l_0 is the initial length of the filament cross section. In the presence of chaotic advection ($\lambda > 0$), exponential growth of the filament cross section is accommodated by striated packing within pores as per Figure 3.

4.2. *Fluid Deformation in 3D Random Networks*

In contrast to ordered 3D networks, the orientation angle θ between pore elements in the model random 3D network follows a Markov process, and so the average stretching rate λ_∞ (Lyapunov exponent) is calculated by Lester *et al.* (2013) as

$$\lambda_\infty = \frac{1}{\pi^2}\int_{-\pi/2}^{\pi/2} d\delta \int_0^{\pi} d\Delta\, \lambda(\delta, \Delta) \approx 0.1178. \tag{4.7}$$

To develop a model of deformation in a random network we consider evolution of an arbitrary infinitesimal material line element $\delta\mathbf{l}$, which evolves with pore number n over the branch and merge elements respectively via the two-step process

$$\delta\mathbf{l}_{2n+1}=\mathbf{R}(\varphi_s)\cdot\mathbf{F}_{\text{2D}}\cdot\mathbf{R}^{-1}(\varphi_s)\cdot\delta\mathbf{l}_{2n},\quad \delta\mathbf{l}_{2n+2}=\mathbf{R}(\varphi_c)\cdot\mathbf{F}_{\text{2D}}^{-1}\cdot\mathbf{R}^{-1}(\varphi_c)\cdot\delta\mathbf{l}_{2n+1},\tag{4.8}$$

where φ_s, φ_c are the orientation angles of the pore branch, merger with respect to the y-direction. For random media, these angles are randomly, independently and uniformly distributed. As such, it is not necessary to resolve the absolute orientation of the line element $\delta\mathbf{l}$, but rather φ_s, φ_c can be re-framed as the orientation angles of the pore branch or merger with respect to the line element without change to (4.8). Henceforth we shall use this definition of φ, and so the length $\delta l=|\delta\mathbf{l}|$ of the line element then evolves via the two-step process

$$\delta l_{2n+1}=\delta l_{2n}\rho_s(\varphi_{2n}),\qquad \delta l_{2n+2}=\delta l_{2n+1}\rho_c(\varphi_{2n+1}),\tag{4.9}$$

where ρ_s, ρ_c respectively are the relative elongations due to stretching and compression within a pore branch and merger derived from (4.2):

$$\rho_s(\varphi_s)=\sqrt{1+3\cos^2\varphi_s},\qquad \rho_c(\varphi_c)=\frac{1}{2}\sqrt{4-3\cos^2\varphi_c}.\tag{4.10}$$

The mean stretching λ_s and compression λ_c rates within a pore branch and merger are then

$$\lambda_s=\frac{1}{2\pi}\int_{-\pi}^{\pi}d\varphi_s\ln[\rho_s(\varphi_s)]\approx 0.4055,\quad \lambda_c=\frac{1}{2\pi}\int_{-\pi}^{\pi}d\varphi_c\ln[\rho_c(\varphi_c)]\approx -0.2877\tag{4.11}$$

and the sum of these stretching rates recovers the infinite-time Lyapunov exponent $\lambda_\infty\approx 0.1178$. The full distribution of stretching rates can be derived from (4.10) as

$$P_{\rho_s}(\rho_s)=\frac{4}{\pi\sqrt{\rho_s^2-1}\sqrt{4-\rho_s^2}},\qquad P_{\rho_c}(\rho_c)=\frac{4}{\pi\sqrt{1-\rho_c^2}\sqrt{4\rho_c^2-1}},\tag{4.12}$$

and the total stretch $\rho:=\rho_s\rho_c$ over a couplet is then distributed as

$$\begin{aligned}P_\rho(\rho)=&\int_{\frac{1}{2}}^{1}d\rho_c'\int_1^2 d\rho_s' P_{\rho_s}(\rho_s')P_{\rho_c}(\rho_c')\delta(\rho-\rho_c'\rho_s'),\\ =&\frac{4}{\pi^2}\left|\frac{\rho}{\rho^2-1}\right|K\left(1-\frac{9\rho^2}{4\rho^2-4}\right),\rho\in[\frac{1}{2},2],\end{aligned}\tag{4.13}$$

where K is the complete elliptic integral of the first kind. To develop an additive process for fluid deformation we consider evolution of the logarithmic length $s:=\ln\delta l$ of a line element, where s evolves over a couplet via the one-step additive process

$$s_{n+2}=s_n+\phi,\tag{4.14}$$

and the stretching increment $\phi=\ln\rho$ is distributed as $P_\phi(\phi)=\exp(\phi)P_\rho(\exp\phi)$, for $\phi\in[-\ln 2,\ln 2]$. Asymmetry of the stretching PDF $P_\phi(\phi)$ for random φ_s, φ_c leads to persistent fluid stretching as shown in Figure 4(b) and reflected by the Lyapunov exponent λ_∞. This asymmetry arises from the basic differences between stretching and compression; within a pore branch stretching is enhanced as the material line rotates toward the maximum stretching direction, whilst compression is retarded in a pore merger due to rotation away from the contraction direction. Hence whilst transverse fluid stretching and compression are equally partitioned in random 3D networks, the asymmetry between stretching and compression generates persistent exponential stretching.

As both the mean λ_∞ and the variance $\sigma^2\approx 0.1144$ of the stretching increment distribution $P_\phi(\phi)$ are bounded, then from the Central Limit Theorem the PDF of the non-dimensional strip elongation $\rho_n = \delta l_n/\delta l_0$ converges to a lognormal distribution

$$\hat{p}_\rho(\rho, n) \approx \frac{1}{\rho\sqrt{\pi n\sigma^2}} \exp\left[-\frac{(\ln\rho - n\lambda_\infty/2)^2}{n\sigma^2}\right], \tag{4.15}$$

which captures convergence of the finite-time Lyapunov exponents $\lambda_n = s_n/n$ toward λ_∞ as per (Lester *et al.* 2013). As material filaments flow through pore branches and mergers in random 3D porous networks, they undergo a series of punctuated stretching and compression events around critical points which leads to net exponential stretching transverse to the mean flow direction.

Note that the PDF (4.15) quantifies the point-wise elongation statistics for an infinitesimal line element. However, when sampling an evolving 1D material line in space, the sampling rate is proportional to the length of the entire 1D line. This is important because the solute concentration statistics are determined by spatial sampling across such a 1D line. The elongation PDF weighted by the length of the entire line, $p_\rho(\rho, n) \propto \rho\hat{p}_\rho(\rho, n)$, is then

$$p_\rho(\rho, n) = \frac{1}{\rho\sqrt{2\pi\sigma^2_{\ln\rho}}} \exp\left[-\frac{(\ln\rho - \mu_{\ln\rho})^2}{2\sigma^2_{\ln\rho}}\right], \tag{4.16}$$

where $\mu_{\ln\rho} = n\Lambda_\infty/2$, $\sigma^2_{\ln\rho} = n\sigma^2/2$ and $\Lambda_\infty := \lambda_\infty + \sigma^2$. Due to issues of non-stationarity and non-linearity of the map $\mathcal{M}$, the values of the mean λ_∞ and variance σ^2 of the stretching distribution $P_\phi(\phi)$ derived contain small errors ($< 10\%$). In Appendix A we derive more accurate values for these parameters ($\lambda_\infty \approx 0.1277$, $\sigma^2 \approx 0.1237$) which are used throughout the rest of this study.

4.3. *Fluid Advection in 3D Random Networks*

The transit time PDF over a pore branch or merger is the same for both elements and is defined by the temporal map $\mathcal{T}$ (3.5) in terms of the radial pore coordinate $r_r^2 = x_r^2 + y_r^2$,

$$\Delta t(r_r) = \frac{\Delta t_a}{1 - r_r^2}, \tag{4.17}$$

where Δt_a is the average residence time within the pore element. As r_r is distributed as $P_r(r) = 2r$ for $r \leq 1$, then the transition time is Pareto distributed as

$$\psi(\Delta t) = \frac{1}{\Delta t_a}\left(\frac{\Delta t}{\Delta t_a}\right)^{-2}, \qquad \Delta t \geq \Delta t_a. \tag{4.18}$$

Note that the Pareto distribution describes the transition times of non-diffusive material fluid elements over a pore-length. Unlike for solute particles, whose transit times is cut-off at the diffusion time over the pore cross-section, this is not the case here. For more complex porous media, pore velocities are often found to align according to exponential or stretched exponential distributions (Moroni & Cushman 2001; Kang *et al.* 2014; Siena *et al.* 2014; Holzner *et al.* 2015). The corresponding transit times shows a similar long time behaviour as (4.18).

5. Stretching Continuous Time Random Walk

To quantify pore-scale mixing in terms of the stretching and advection dynamics considered above, we propose to represent the stochastic stretching process as a random walk in the space of time and elongation. As the orientation angles φ_s, φ_c for the pore branch and merge elements are random, the elongation rates are uncorrelated across successive pores. Hence, the successive material line elongations follow a Markov process defined by equation (4.9). Similarly, because of the random re-orientation, the travel times across successive pores are also weakly correlated (Lester *et al.* 2013). Hence both the series of elongations and the travel times follow Markov processes in space. This implies that the deformation of a fluid material element can be modelled as a Continuous Time Random Walk (CTRW), whereby fluid elements undergo a series of punctuated stretching and compression events occurring in random times as they propagate through the pore network. Whilst most CTRW models consider random spatial increments in random times to model spatial transport processes, we develop a stretching CTRW model that considers random elongation events occurring in random times to represent the stochastic stretching process.

The approach we shall employ to model fluid mixing is to consider both the deformation and advection of an infinitesimal fluid element in the absence of diffusion as random walk processes conditioned upon the transport dynamics derived in the previous Section. We then account for molecular diffusion by utilizing the deformation history in the CTRW to solve a local ADE, and the ensemble of such elements informs the evolution of the concentration PDF in the pore space. Note that as diffusion is fully coupled to deformation we account explicitly for stretching enhanced diffusion.

The two-step stretching process (4.9) over a couplet provides a natural discretization for a CTRW of fluid deformation, and the temporal map $\mathcal{T}$ also quantifies residence time. For this random walk model we do not need to resolve the particle location in terms of pore space coordinates (x_r, y_r), but rather only consider the distributions of the travel time Δt and stretch ρ_s, ρ_c derived from the relationships in Section 4. The resultant two-step CTRW over a couplet is then

$$\delta l_{2n+1} = \delta l_{2n} \rho_s(\varphi_{2n}), \qquad t_{2n+1} = t_{2n} + \Delta t_{2n}, \tag{5.1a}$$

$$\delta l_{2n+2} = \delta l_{2n+1} \rho_c(\varphi_{2n+1}), \qquad t_{2n+2} = t_{2n+1} + \Delta t_{2n+1}, \tag{5.1b}$$

where the advection time between pore elements Δt_n is distributed as $\psi(\Delta t)$ (4.18), and the random alignment angles φ_{2n}, φ_{2n+1} are uniformly distributed over $[-\pi, \pi]$. Thus, the stretching CTRW quantifies the elongation of the length δl_n of a material element at subsequent downstream positions z_n, and the deformation time through the temporal random walk t_n. For simplicity we approximate the deformation rates during a stretching or compression transition as being constant. Whilst the multiplicative two-step nature of the CTRW (5.1) does not permit analytic solution, analytic solutions are possible for an equivalent additive one-step CTRW over a couplet in terms of $s = \ln \delta l$

$$s_{2n+2} = s_{2n} + \phi_{2n}, \qquad t_{n+2} = t_{2n} + \Delta t_{2n} + \Delta t_{2n+1}. \tag{5.2}$$

Note that the fluid stretching for this one-step CTRW is not uniform over a couplet, but rather is oscillatory due to stretching and compression over a pore branch or merger respectively. Whilst such oscillations do not impact the overall stretching rate λ_∞, such oscillatory stretching may generate a significant diffusive signature over the couplet. We shall return to this issue in §6 where we develop a pore-scale mixing model based upon this one-step CTRW (5.2).

6. Scalar Mixing and Fluid Stretching CTRW

To model pore-scale solute mixing we employ a 1D lamellar mixing model (Ranz 1979; Duplat & Villermaux 2008; Le Borgne *et al.* 2015), where fluid stretching is quantified

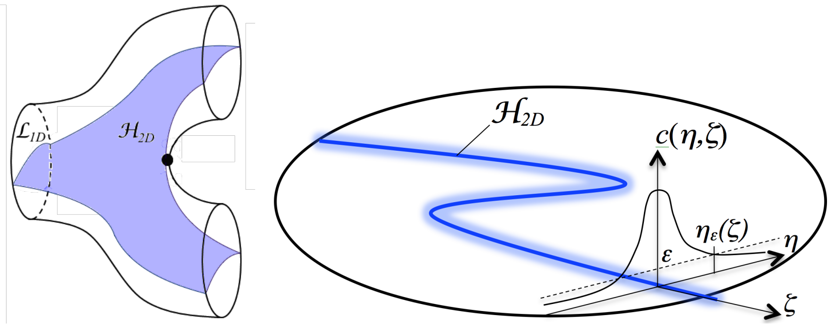

(a) (b)

FIGURE 5. (a) Schematic of the *lamella* formed by the 2D material sheet $\mathcal{H}_{2D}$ arising from continuous injection of a 1D material line in the inlet plane (b). The lamellae $\mathcal{H}_{2D}$ (solid blue line) forms the backbone of the diffusive concentration field $c(\mathbf{x})$ (blurred blue region), shown here intersecting a pore outlet in the xy-plane, injected along the same material line in the inlet plane, resulting in a Gaussian concentration distribution transverse to $\mathcal{H}_{2D}$. Here (η,ζ) are the material coordinates normal and tangential to $\mathcal{H}_{2D}$ in the xy-plane.

by the CTRW model developed in §5. Due to exponential fluid stretching, an evolving concentration field conforms to a highly striated lamellar structure, where these lamellae align with the dominant stretching direction(s) of the flow and are simultaneously stretched longitudinally and compressed transversely.

The continuous injection of a 1D material line $\mathcal{L}_{1D}$ of length l_0 across a single pore of the inlet plane ($z=n=0$) of the 3D network forms a continuous 2D material sheet $\mathcal{H}_{2D}$ shown in Figure 5(a) which propagates throughout the pore space of the network and branches into multiple pores. We denote this 2D material sheet $\mathcal{H}_{2D}$ as a single *lamella*, and define the material coordinates $\{\eta,\zeta\}$ in the xy-plane where ζ is the coordinate along the lamella and η is the transverse coordinate. We consider the steady concentration field $c(\mathbf{x})=c(\eta,\zeta,z)$ which arises from the continuous injection of a concentration strip along the 1D material line $\mathcal{L}_{1D}$ with a Gaussian transverse profile

$$c(\eta,\zeta,0)=\frac{c_0}{\sqrt{2\pi\sigma_0^2}}\exp\left(-\frac{\eta^2}{2\sigma_0^2}\right), \tag{6.1}$$

with maximum initial concentration $c_m(0)=c_0/\sqrt{2\pi\sigma_0^2}$ and variance σ_0^2. As shown in Figure 5(b) the lamella $\mathcal{H}_{2D}$ then forms the ridge of the 3D solute concentration field $c(\mathbf{x})$ throughout the pore network, and the concentration transverse to $\mathcal{H}_{2D}$ follows a Gaussian profile. For simplicity of exposition we consider a uniform solute injection applied at the inlet plane $z=0$ across the entire network. This means, we assume the same "initial" concentration profile (6.1) across the lamellae in all pores located at the inlet plane at $z=0$. Thus, the composition of the concentration field does not depend on the position transverse to the mean flow direction and only depends on the longitudinal distance z. We shall extend these results in §7 to the case of a heterogeneous solute injection across the inlet plane.

The macroscopically homogeneous initial condition described above results in an ensemble of 2D lamellae $\mathcal{H}_{2D}$ which are homogeneously distributed throughout the pore network. Hence lamellae segments from different inlet pores may coexist within a single pore, and the spacing between lamellae segments decays in the longitudinal direction as the exponential stretching rate, however these segments never overlap due to their invariant nature. Conversely, the associated 3D concentration field $c(\mathbf{x})$ has finite width and so will eventually overlap and coalescence. Whilst a pore may contain segments of different lamellae, this re-distribution of lamellar segments between pores does not impact the concentration distribution at a statistical level due to the homogeneous inlet condition described above. Hence the statistical concentration distribution is the same across all pores for fixed n and we do not need to resolve the re-distribution of lamellar segments across pores. This homogeneous inlet condition greatly simplifies exposition of the method, but in principle may be extended to inhomogeneous inlet conditions by explicitly tracking this re-distribution, facilitating solution of both the evolving pore-scale and macroscopic concentration distributions throughout the network.

The steady 3D concentration field $c(\mathbf{x})$ in the network is governed by the steady ADE

$$-\mathbf{v}(\mathbf{x})\cdot\nabla c(\mathbf{x})+D_m\nabla^2 c(\mathbf{x})=0,\quad \nabla c(\mathbf{x})\cdot\mathbf{n}|_{\partial\mathcal{D}}=0, \tag{6.2}$$

where D_m is molecular diffusivity and $\mathbf{n}$ is the outward normal from the boundary $\partial\mathcal{D}$. Under the assumption that the spatial concentration gradients are small in the z-direction, we ignore longitudinal diffusion and pose the steady 3D ADE (6.2) as an equivalent unsteady 2D ADE in the xy-plane

$$\frac{\partial c}{\partial t}=v_z\frac{\partial c}{\partial z}=-\mathbf{v}_\perp(x,y,t)\cdot\nabla_\perp c(x,y,t)+D_m\nabla_\perp^2 c(x,y,t), \tag{6.3}$$

where v_z is the z-component of $\mathbf{v}(\mathbf{x})$ and $\perp$ denotes the xy-components. The z-coordinate is also parameterised in terms of the Lagrangian travel time $t=t(z)$ along a fluid particle trajectory as

$$t(z)=\int_0^z dz'\frac{1}{v_z(z')}. \tag{6.4}$$

The lamellar mixing model is based upon posing (6.3) in terms of the material coordinates $\{\eta,\zeta\}$ in the xy-plane, hence $c(x,y,t)\mapsto c(\eta,\zeta,t)$. Under exponential fluid stretching, concentration gradients along the lamella (∂_ζ) decay exponentially whilst the gradients normal to the lamella (∂_η) are maintained, thus level sets of the concentration field identify with the lamella. This alignment occurs regardless of the inlet condition, and so the lamellar approach is quite generic. Under these conditions the ADE (6.3) simplifies to the 1D lamellar transport equation (Ranz 1979; Duplat & Villermaux 2008; Villermaux 2012; Le Borgne *et al.* 2013)

$$\frac{\partial}{\partial t}c(\eta,\zeta,t)=\gamma(t,\zeta)\eta\frac{\partial}{\partial\eta}c(\eta,\zeta,t)+D_m\frac{\partial^2}{\partial\eta^2}c(\eta,\zeta,t), \tag{6.5}$$

where the stretching rate $\gamma(t,\zeta)\equiv\partial_\zeta v_\zeta=-\partial_\eta v_\eta$ arises from a first order expansion of the η-component of the velocity field, and the stretching rate $\gamma(t,\zeta)$ can be expressed in terms of the lamella elongation in the xy-plane $l(t,\zeta)$ as

$$\gamma(t,\zeta)\equiv\frac{\partial v_\zeta}{\partial\zeta}=\frac{d\ln l(t,\zeta)}{dt}. \tag{6.6}$$

Note that the 1D nature of (6.5) renders it only valid up to the coalescence of lamellae in the pore-space. Whilst methods (Duplat & Villermaux 2008; Villermaux 2012; Le Borgne *et al.* 2013) exist to extend beyond coalescence and are readily applicable to this problem, they are beyond the scope of this present study.

Due to negligible transport in the ζ direction, (6.5) can be posed with respect to a single fluid element trajectory within the lamella, and describes evolution of the associated transverse concentration $c(\eta,t)$ profile as

$$\frac{\partial}{\partial t}c(\eta,t)=\gamma(t)\eta\frac{\partial}{\partial\eta}c(\eta,t)+D_m\frac{\partial^2}{\partial\eta^2}c(\eta,t), \tag{6.7}$$

This particle-based description of fluid mixing is compatible with the CTRW stretching model. As such, we do not seek to directly solve the evolution of an entire lamella, but rather solve the evolving concentration profile $c(\eta, t_n)$ over a representative ensemble of points which recovers the same statistics of the ensemble of all lamellae in the pore-space due to ergodicity.

If we consider fluid advection and stretching as stochastic processes, then for given z_n or n the advection time $t_n = t(z_n)$ is distributed randomly according to the waiting time distribution (4.18). Hence $c(\eta, t_n)$ is a random variable through its dependence on both the random advection time t_n and random deformation $\gamma_n = \gamma(t_n)$. Under the assumption of independent lamellae, the PDF of concentration at a cross-section at z_n is obtained by (i) sampling the concentration values across the lamella, and (ii) sampling between the lamellae. This interpretation allows the lamellar mixing equation (6.7) to describe evolution of the transverse concentration profile with advection time and stretching history of any part of any lamellae in the the entire 3D porous network.

We non-dimensionalise (6.7) by introducing the variables $c' = c/c_m(0)$, $t' = t/\Delta t_a$, $\eta' = \eta/(\sqrt{2}\sigma_0)$, with the characteristic advection time $\Delta t_a = \ell/v_0$, where ℓ is the length of a pore and v_0 the mean pore velocity. We also define the Péclet number as $Pe = \sigma_0^2 v_0/(2D_m\ell)$, and henceforth drop the primes for simplicity of notation. Under these scalings (6.7) is non-dimensionalized with D_m now replaced by $1/Pe$ and the initial condition (6.1) is now $c(\eta, 0) = \exp(-\eta^2)$. To solve (6.7), follwing Ranz (1979) we define the reduced coordinate η_0 and operational time $\tau(t)$ respectively as

$$\eta_0(t) = \eta\rho(t), \qquad \tau(t) = \int_0^t dt'\rho(t')^2, \tag{6.8}$$

where the solution $c(\eta, t) = g[\eta_0(t), \tau(t)]$ is equivalent to a transformation into the characteristic system of (6.7). Making this substitution, (6.7) simplifies to the diffusion equation

$$\frac{\partial g(\eta_0, \tau)}{\partial \tau} = Pe\frac{\partial^2 g(\eta_0, \tau)}{\partial \eta_0^2}, \tag{6.9}$$

with initial condition $g(\eta_0, 0) = \exp(-\eta_0^2)$. Hence the concentration profile $c(\eta, t) = g[\eta_0(t), \tau(t)]$ across the strip is given by the Gaussian distribution

$$c(\eta, t) = \frac{1}{\sqrt{1 + \frac{\tau(t)}{Pe}}} \exp\left(-\frac{\eta^2\rho(t)^2}{1 + \frac{\tau(t)}{Pe}}\right), \tag{6.10}$$

and so the concentration profile is determined by the total stretch $\rho(t)$ which acts to narrow lamellae and the stretching history $\tau(t)$ which broadens and dilutes the lamellae. As $\tau(t)$ depends upon the stretching history, stretching oscillations in the two-step process (5.1) over a couplet are captured by $\tau(t)$, and so must be accounted for if significant. From (6.10) the maximum concentration $c_m(t) = c(0, t)$ is now

$$c_m(t) = \frac{1}{\sqrt{1 + \frac{\tau(t)}{Pe}}}. \tag{6.11}$$

Equations (6.8)-(6.11) show that pore-space mixing explicitly depends upon Pe and the stretching history $\rho(t)$ which is used to encode the operational time $\tau(t)$. The fluid deformation CTRW model developed in § 4 yields expression (4.16) for the PDF of $\rho(t_n)$, and so this must be extended to generate analytic expressions for the PDF of $\tau(t_n)$, the concentration PDF and associated measures.

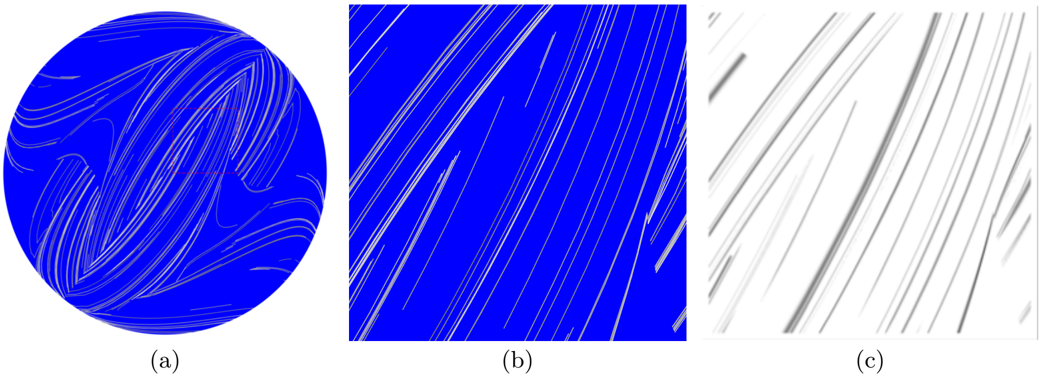

FIGURE 6. (a) Typical distribution of the logarithm of operational time $\ln \tau$ (black, $\ln \tau = 50$, white $\ln \tau = 5$) representing the backbone of the lamellar concentration field, with detail (dashed box) shown in (b). The associated scalar field $c(\mathbf{x})$ for $Pe = 10^8$ shown in (c) is calculated via the diffusive strip method (Meunier & Villermaux 2010).

Equations (6.8)-(6.11) also form the basis of the diffusive strip method (Meunier & Villermaux 2010) which facilitates efficient numerical solution of the 1D lamellar ADE (6.7) across a broad range of Pe. To test the accuracy of the analytic solutions for the concentration PDF described above, we employ this method in conjunction with the advective $\mathcal{M}$ and temporal $\mathcal{T}$ maps to simulate deformation of a 2D material filament within the 3D pore-space. Diffusion is calculated as a post-processing step for various Pe via (6.10) given computation of ρ and τ along the strip from the stretching history. This method is capable of accurately capturing stretching, diffusion and coalescence of the scalar field up to $n \sim 100$ pores, beyond which exponential growth of the lamellar structure is too large for feasible computation. Figure 6 shows a typical distribution of the operational time $\ln \tau$ over the cross-section of a pore at $n = 40$ using this method, as well as the concentration distribution$c(\mathbf{x}, t_n)$ calculated at $Pe = 10^8$.

In order to obtain a closed form expression for the PDF of $\tau(t_n)$ from the CTRW model, we approximate evolution of $\rho(t)$ between $t = 0$ and $t = t_n$ as a constant exponential stretching process

$$\rho(t) \approx \exp\left(\Gamma_n t\right) \tag{6.12}$$

in terms of the average stretching rate $\Gamma_n = \ln(\rho_n)/t_n$ after n steps. From (6.12), the operational time $\tau(t_n)$ is then approximated as

$$\tau_n \equiv \tau(t_n) \approx \frac{t_n \rho_n^2}{2\ln(\rho_n)}. \tag{6.13}$$

This expression can be further simplified by noticing that the PDF (4.16) of $\ln(\rho_n)$ is Gaussian, with mean $n\Lambda_\infty/2$ and variance $n\sigma^2/2$. Thus, we may approximate the denominator in (6.13) by its mean value $\ln(\rho_n) \approx n\Lambda_\infty/2$

$$\tau_n \approx \frac{t_n \rho_n^2}{n\Lambda_\infty}, \tag{6.14}$$

the accuracy of which is shown in Figure 7(a). In essence, (6.14) solves the pore-scale fluid mixing, involving exponential growth of τ_n with n. Oscillations associated with the two-step stretching process (5.1) appear to play a minor role as τ_n is well-approximated by the one-step stretching process (5.2) characterized in terms of the mean stretching rate Λ_∞, as reflected by Figure 7(a). Thus, whilst in principle diffusion is dependent

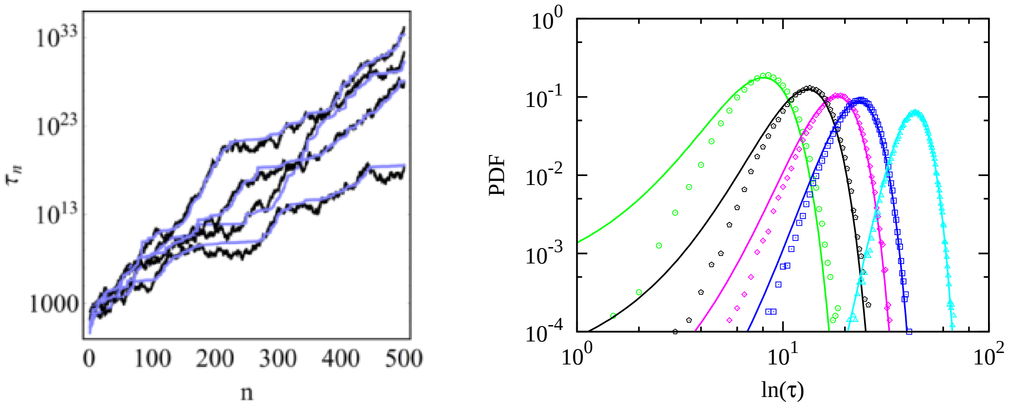

(a) (b)

FIGURE 7. (a) Comparison of direct computation (black) and analytic approximation (6.14) (blue) for operational time τ_n with pore number n over four different realizations of the CTRW model. (b) Comparison of the PDF of $\ln\tau$ based upon the analytic approximation (6.16) (solid lines), the PDF of $\ln\tau$ from the CTRW model for (circles) $n = 20$, (pentagons) $n = 40$, (diamonds) n = 60, (squares) $n = 80$, (triangles) $n = 160$.

upon the entire stretching history, it is predominantly governed by the arrival time t_n of the material strip at position z_n and the elongation ρ_n. The travel time distribution over a single pore is given by the Pareto distribution (4.18). The distribution of the arrival times t_n is given by the self-convolution of the Pareto distribution, which results into a Landau distribution. In Appendix B we show explicilty that the bulk of the Landau distribution can be well approximated by the Moyal distribution.

The PDF of $\ln(\tau_n) = \ln(t_n) + 2\ln(\rho_n) - \ln(n\Lambda_\infty)$ is well approximated by replacing $\ln(t_n)$ with its average

$$\langle \ln t_n \rangle \approx \ln\left[\frac{n}{a}\left(\ln 2 + \gamma + b\right) + n\left(\ln n + 1 - \gamma\right)\right], \tag{6.15}$$

where γ is the Euler-Mascheroni constant, $a = 0.7413$, $b = 0.0064$ (Appendix B). Due to the Central Limit Theorem, $\ln(\rho_n)$ converges with n toward the Gaussian distribution (4.16) with the mean $n\Lambda_\infty/2$ and variance $n\sigma^2/2$, and so the PDF of $\xi_n := \ln(\tau_n)$ also converges with n toward the Gaussian distribution

$$p_{\ln\tau}(\xi, n) = \frac{\exp\left(-\frac{[\xi - \mu_{\ln\tau}(n)]^2}{2\sigma_{\ln\tau}^2(n)}\right)}{\sqrt{2\pi\sigma_{\ln\tau}^2(n)}} \tag{6.16}$$

with mean and variance

$$\mu_{\ln\tau}(n) = \langle \ln(t_n) \rangle + n\Lambda_\infty - \ln(n\Lambda_\infty), \qquad \sigma_{\ln\tau}^2(n) = 2n\sigma^2. \tag{6.17}$$

Figure 7(b) shows that for $\tau > 10^3$ the approximation (6.16) exhibits very good agreement with the PDF of ξ_n obtained from evaluating $\tau(t_n)$ according to (6.8) with $\rho(t_n)$ given by the CTRW (5.1). The mismatch at short times is expected due to the asymptotic nature of the Central Limit Theorem.

7. Chaotic Mixing in 3D Random Porous Media

The approximation (6.16) for τ_n provides an accurate solution to the two-step CTRW (5.1), which along with the distribution (4.16) for ρ_n quantifies evolution of the concen-

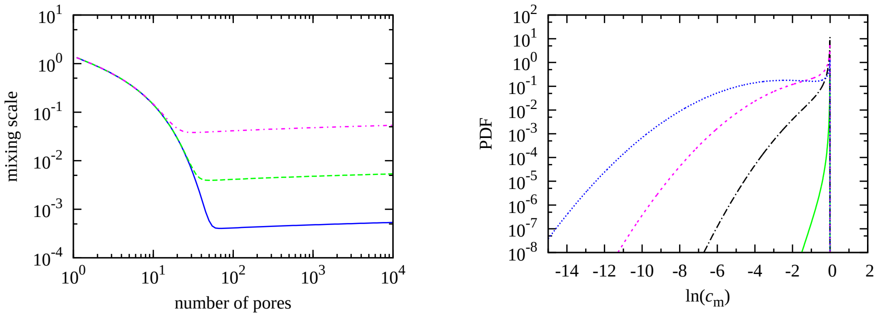

(a) (b)

FIGURE 8. (a) Evolution of the average mixing scale (7.3) with n for (dash-dotted) $Pe = 10^4$, (dashed) $Pe = 10^6$ and (solid) $Pe = 10^8$. (b) PDF (7.6) of $\ln c_m$ at downstream positions of (solid) $n = 20$, (dash-dotted) $n = 40$, (long dashed) $n = 60$ and (short dashed) $n = 80$ for $Pe = 10^8$.

tration distribution, mixing and dilution in the 3D open porous network prior to the onset of coalescence. In the following we apply this solution to determine evolution of the mixing scale, concentration PDF, maximum concentration, scalar variance and the onset of coalescence in the 3D random porous network.

7.1. *Mixing Scale and Onset of Coalescence*

The mixing scale ϵ_m characterizes the distribution of lamellae widths at $z_n = n$ as

$$\epsilon_m(n) = \frac{\int_{-\infty}^{\infty} d\eta|\eta|c(\eta, t_n)}{\int_{-\infty}^{\infty} d\eta c(\eta, t_n)} = \frac{\sqrt{(1+\tau_n/Pe)}}{\pi\rho_n}, \tag{7.1}$$

the average of which is well approximated by substitution of (6.14) for τ_n for the Landau distribution as outlined in Appendix B.

$$\langle \epsilon_m(n)\rangle \approx \left\langle \sqrt{\frac{\langle t_n\rangle + Pe\,\rho_n^{-2}}{\pi n Pe \Lambda_\infty}} \right\rangle . \tag{7.2}$$

Note that whilst $\langle t_n\rangle$ is strictly infinite, the above average is dominated by the bulk of $p_n(t)$, which, as outlined in Appendix B can be well approximated by the Moyal distribution. In order to perform the average over ρ_n, we use Laplace's method (Erdélyi 1956) to evaluate the corresponding integral, which yields

$$\langle \epsilon_m(n)\rangle \approx \sqrt{\frac{\ln n}{\pi Pe \Lambda_\infty}} \sqrt{1 + \frac{\ln 2 + \gamma + b}{a \ln n} + \frac{1-\gamma}{\ln n} + \frac{Pe\exp(-\Lambda_\infty n)}{n \ln n}}. \tag{7.3}$$

This is a remarkable result because although fluid elements grow exponentially with longitudinal pore number n, the mixing scale ϵ_m does not converge to a constant Batchelor scale with in, but as shown in Figure 8, rather ϵ_m reaches a minimum at

$$n_c \approx \frac{\ln(Pe\Lambda_\infty)}{\Lambda_\infty}, \tag{7.4}$$

and then increases asymptotically as $\langle \epsilon_m(n)\rangle \approx \sqrt{\ln n/(\pi Pe\Lambda_\infty)}$. This non-monotonic behaviour is driven by the broad distribution of arrival times between the couplets arising from the no-slip condition, which renders a distribution of stretching rates of variable strength. Note that the characteristic waiting time between stretching events increases with the number of couplets, and thus the stretching rate decreases. This is a characteristic of the Pareto transit time distribution. As such, we identify transport in the region $n \leq n_c$ as *advection-dominated* where compression of concentration filaments dominates due to stretching of lamellae, whereas for $n > n_c$ transport is *diffusion-dominated*, leading to diffusive spreading of the concentration profile transverse to lamellae. Note that these results apply even if concentration filaments have not yet coalesced.

Whilst such prediction is beyond the scope of this study, it is important to determine the onset of coalescence and hence the envelope of validity of the model. The onset of coalscence occurs when the mixing scale $\langle\epsilon_m(n)\rangle$ exceeds the average spacing $\epsilon(n) = \pi R^2/l(n)$ between lamellae of length $l(n) = l_0\exp(\lambda_\infty n)$ with an initial length l_0 in pores of average radius R. From (7.3), the lamellae are non-interacting up to pore number

$$n + \frac{1}{2\lambda_\infty}\ln\ln n \leqslant \frac{1}{\lambda_\infty}\ln\left(\frac{\pi R^2}{l_0\sigma_0}\sqrt{\frac{\pi Pe\Lambda_\infty}{2}}\right), \tag{7.5}$$

where the linear contribution on the LHS of (7.5) is due to exponential stretching of the lamellae, and the weaker nonlinear term is due to evolution of the mixing scale $\langle\epsilon_m(n)\rangle$.

7.2. *PDF of Maximum Concentration*

The dimensionless maximum concentration $c_m(t)$ as a function of pore number n, $c_m(n) = c_m(t_n)$ is given by (6.11). In order to develop an analytic expression for the PDF of $c_m(n) = c_m(t_n)$, we express (6.11) as a function of $\xi_n = \ln(\tau_n)$, which is distributed according to (6.16) as $\xi_n = \ln\left(Pe\left[c_m(n)^{-2} - 1\right]\right)$. Hence the PDF of $\zeta_n = \ln[c_m(n)]$ is

$$p_{\ln c_m}(\zeta, n) = \frac{2}{1-\exp(2\zeta)}p_{\ln\tau}\left[\ln\left(Pe\left[\exp(-2\zeta) - 1\right]\right)\right]. \tag{7.6}$$

For $|\zeta| \gg 1$ the PDF of ζ is well approximated by a Gaussian distribution, as per Figure 8(b) which shows the PDF of $\ln c_m$ for $Pe = 10^8$. For small $n \leq 40$, the PDF is sharply peaked about the initial concentration $c_m = 1$, but for $n > 40$ a peak starts forming away from $c_m = 1$ and the bulk of the probability weight moves away from this initial concentration. This behaviour is reflected by evolution of the mixing scale with n, which assumes its minimum at n_c (7.4), which for the $Pe = 10^8$ chosen here is $n_c \approx 70$. Thus, once the mixing scale assumes its minimum value, dilution increases markedly due to increased diffusive mass transfer. The average maximum concentration $\langle c_m(n)\rangle$ shown in Figure 9 evolves in a similar manner; in the advection-dominated regime ($n < n_c$) $\langle c_m(n)\rangle$ is essentially equal to the initial concentration of 1, whereas in the diffusion-dominated regime $n \gg n_c$, it decays exponentially rapidly according to

$$\langle c_m(n)\rangle \approx \exp\left[\frac{\sigma^2_{\ln\tau}(n)}{8} - \frac{\mu_{\ln\tau}(n) - \ln Pe}{2}\right], \tag{7.7}$$

where $\mu_{\ln\tau}$ and $\sigma^2_{\ln\tau}$ are given by (6.17). Hence once the diffusion-dominated regime ($n \gg n_c$) is reached, exponential fluid stretching due to chaotic advection in 3D porous media generates exponential dilution. Chaotic advection exponentially increases concentration gradients and so effectively shortens the advection-dominated regime, as reflected by (7.4) which shows that n_c decreases with increasing Lyapunov exponent λ_∞.

In contrast, fluid deformation in 2D porous media is limited to algebraic stretching. In such media Le Borgne *et al.* (2015) and Dentz *et al.* (2015) find that the mean and variance of $\ln\rho$ reflect such algebraic stretching

$$\mu_{\ln\rho,2\text{D}}(n) = \alpha\ln(n+1) + \sigma^2_{\ln\rho,2\text{D}}(n), \qquad \sigma^2_{\ln\rho,2\text{D}}(n) = \beta\ln(n+1), \tag{7.8}$$

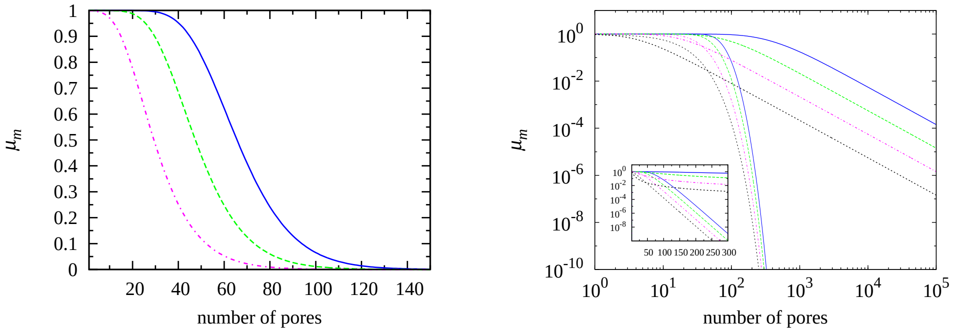

(a) (b)

FIGURE 9. Evolution of the average maximum concentration with n for (dash-dotted) $Pe = 10^4$, (dashed) $Pe = 10^6$ and (solid) $Pe = 10^8$ in (a) linear and (b) log-log axes. In (b) the thin lines indicate the $3D$ pore mixing model, the thick lines, the $2D$ pore mixing model (7.8)–(7.9) with $\alpha = 1$ and $\beta = 1/5$. The inset illustrates the same plot in a semi-logarithmic scale.

where $\alpha, \beta \in [1/2, 2]$. As the derivation leading to (6.16) also holds for algebraic deformation, the mean and variance of the Gaussian $\ln \tau_n$ PDF in 2D porous media are

$$\mu_{\ln \tau,2\mathrm{D}}(n) = \langle \ln(t_n) \rangle + 2\mu_{\ln \rho,2\mathrm{D}}(n) - \ln[2\mu_{\ln \rho,2\mathrm{D}}(n)], \quad \sigma^2_{\ln \tau,2\mathrm{D}}(n) = 4\sigma^2_{\ln \rho,2\mathrm{D}}(n), \tag{7.9}$$

and from (7.7), we obtain the asympotic algebraic decay of average maximum concentration as $\langle c_{m,2\mathrm{D}}(n) \rangle \propto n^{-\alpha - \frac{\beta+1}{2}}$. Hence there exists a qualitative difference in fluid mixing between 2D and 3D porous media: in 2D media fluid stretching is constrained to be algebraic, leading to algebraic dilution, whereas exponential stretching is inherent to 3D porous media, yielding dilution which scales exponentially with longitudinal distance.

7.3. *Concentration PDF, Mean and Variance*

We also derive the pore-scale concentration PDF, mean and variance as a function of the longitudinal pore number n. In terms of the spatial concentration PDF, there exist two different measures which are used to measure, predict and quantify mixing and dilution. The first measure, termed the *fluid support* PDF considers the concentration PDF over the entire fluid cross-sectional area A at a fixed longitudinal distance z_n. The second measure, termed the *concentration support* PDF considers a subset A_c of the area A corresponding to concentration values greater than a minimum threshold ϵ. We shall derive expressions for both concentration measures.

To determine the concentration support PDF, we note that the concentration PDF across a lamella for a given maximum concentration c_m is obtained from (6.10) through spatial mapping over $c \in [\epsilon, c_m]$ as

$$p(c|c_m) = \frac{1}{2c\sqrt{\ln(c_m/\epsilon)\ln(c_m/c)}}, \qquad p(c,n) = \int_c^\infty dc_m p(c|c_m) p_m(c_m,n), \tag{7.10}$$

which, using (7.6) and (7.10), may be expressed in terms of the PDF (6.16) of $\ln \tau$ as

$$p(c,n) = \int_{\ln c}^{\infty} dz \frac{1}{1-\exp(2z)} \frac{p_{\ln \tau}\left[\ln\left(Pe\left[\exp(2z)-1\right], n\right)\right]}{c\sqrt{(z-\ln\epsilon)(z-\ln c)}}, \tag{7.11}$$

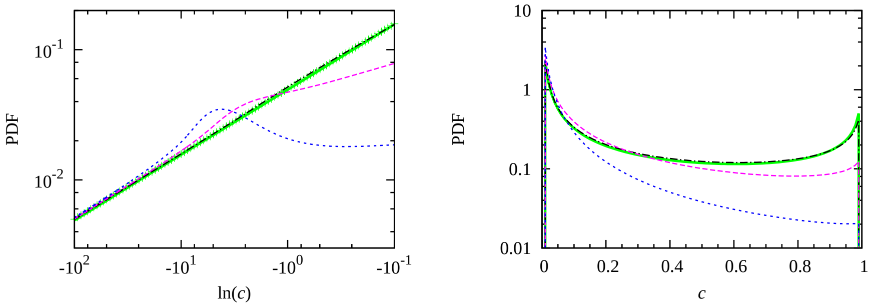

FIGURE 10. Concentration support PDF of (left panel) $\ln c$ and (right panel) c at downstream positions of (solid) $n = 20$, (dash-dotted) $n = 40$, (long dashed) $n = 60$ and (short dashed) $n = 80$ pores for $Pe = 10^8$.

which may be simplified via Laplace's method for $c < \langle c_m(n)\rangle$ to

$$p(c,n) \approx \frac{1}{2c\sqrt{(\ln\langle c_m(n)\rangle - \ln\epsilon)(\ln\langle c_m(n)\rangle - \ln c)}}, \tag{7.12}$$

the k-th moment of which is then

$$\langle c(n)^k\rangle = \frac{\langle c_m(n)\rangle^k \sqrt{\pi}\,\mathrm{erf}\left[\sqrt{k\ln(\langle c_m(n)\rangle/\epsilon)}\right]}{2\sqrt{k\ln(\langle c_m(n)\rangle/\epsilon)}}. \tag{7.13}$$

Figure 10 shows the concentration support PDFs of $\ln c$ and c from (7.12) for $Pe = 10^8$ as a function of longitudinal pore number n. The concentration PDF follows the same trend as that for maximum concentration in that the PDFs for $n = 20$ and 40 are almost indistinguishable due to limited dilution in the advection dominated regime $n \leq n_c$ (where $n_c \approx 70$ for $Pe = 10^8$), whereas significant dilution arises in the diffusion-dominated regime $n > n_c$ after the mixing scale reaches its minimum.

We denote the k-th moment of the spatial concentration PDF under the concentration and fluid supports respectively as

$$\langle c(n)^k\rangle \equiv \frac{1}{A_c}\int_{A_c} d\mathbf{x}\, c(x,y,n)^k, \tag{7.14}$$

$$\overline{c(n)^k} \equiv \frac{1}{A}\int_{A} d\mathbf{x}\, c(x,y,n)^k \approx \frac{1}{A}\int_{A_c} d\mathbf{x}\, c(x,y,n)^k, \tag{7.15}$$

and so for $\epsilon \ll c_m$ these moments are related as

$$A\,\overline{c(n)^k} \approx A_c\langle c(n)^k\rangle. \tag{7.16}$$

From (7.13), under the assumption $\langle c_m(n)\rangle \gg \epsilon$ the concentration support mean and variance are then

$$\langle c(n)\rangle \approx \frac{\langle c_m(n)\rangle\sqrt{\pi}}{2\sqrt{\ln(\langle c_m(n)\rangle/\epsilon)}}, \tag{7.17}$$

$$\sigma^2_{\langle c\rangle}(n) \equiv \langle c(n)^2\rangle - \langle c(n)\rangle^2 = \langle c(n)\rangle^2\left(\frac{\langle c_m(n)\rangle}{\langle c(n)\rangle\sqrt{2}} - 1\right), \tag{7.18}$$

which respectively scale as $\langle c_m(n)\rangle$, $\langle c_m(n)\rangle^2$. Due to conservation of mass the fluid support mean concentration $\overline{c(n)}$ is constant, and is given in dimensional terms by integration of (6.1) for $\epsilon \ll c_m(0)$ as

$$\overline{c(n)} = \frac{1}{A}\int_0^{l_0} d\zeta \int_{-\eta_\epsilon}^{\eta_\epsilon} d\eta\, c(\eta,\zeta,0) \approx \frac{c_0 l_0}{A}, \tag{7.19}$$

where $c|_{\eta=\pm\eta_\epsilon} = \epsilon$. Using (7.16)-(7.18) the fluid support concentration variance scales linearly with $\langle c_m(n)\rangle$ as

$$\sigma^2_{\overline{c}}(n) \equiv \overline{c(n)^2} - \overline{c(n)}^2 = \overline{c(n)}^2\left(\frac{\langle c_m(n)\rangle}{\overline{c(n)}\sqrt{2}} - 1\right). \tag{7.20}$$

Although (7.18), (7.20) yield negative concentration variances in the homogenization limit of large n (as $\langle c_m(n)\rangle \to \langle c(n)\rangle, \overline{c(n)}$), the derived model is valid in the pre-coalescence regime, and so is not expected to capture the late time dissipation dynamics. Conversely, at earlier times when $\langle c_m(n)\rangle \gg \overline{c(n)}, \langle c(n)\rangle$, the pore-scale concentration and fluid support measures of concentration variance respectively scale as $\langle c_m(n)\rangle^2$, $\langle c_m(n)\rangle$, and so directly inherit the behaviour of the maximum concentration $c_m(n)$ for both 2D and 3D porous media. In the diffusion-dominated regime ($n > n_c$) this yields exponential scalar dissipation with pore number n for 3D porous media and algebraic dissipation in 2D media.

7.4. *Chaotic Mixing within an Arbitrary Plume*

Whilst the results above pertain to pore-scale mixing of a macroscopically homogeneous concentration field, we also consider how these results apply to dilution within an arbitrary solvent plume. For illustration we consider a steady plume arising from a continuously injected point source as shown in Figure 3. For such a plume the mean macroscopic concentration develops a Gaussian distribution in the direction transverse to the mean flow. Hence, the average lamellar length l_p per pore varies with the transverse radial r and longitudinal $z_n = \ell n$ distance from the injection source point as

$$l_p(n,r) = \frac{l(n)}{\pi n^2 d^2}\exp\left(-\frac{(\phi_A r)^2}{n^2 d^2}\right), \tag{7.21}$$

where the total lamellar length is $l(n) = l_0\exp(\lambda_\infty n)$, ϕ_A is the transverse areal porosity, and d pore inlet/outlet centre-to-centre distance.Pore-scale concentration support measures such as the mean mixing scale $\langle\epsilon_m(n)\rangle$, maximum concentration $\langle c_m(n)\rangle$, concentration PDF $p(c|n)$, concentration mean $\langle c(n)\rangle$ and variance $\sigma^2_{\langle c\rangle}(n)$ under the concentration support are the same as for point-wise or uniform injection, the concentration mean $\overline{c(n)}$ and variance $\sigma^2_{\overline{c}}(n)$ under the fluid support are markedly different. Following (7.17) and (7.18), these pore-scale quantities within the plume vary with pore number n and radial distance r as

$$\overline{c_p(n,r)} = \overline{c(n)}\frac{l_p(n,r)}{l(n)}, \tag{7.22}$$

$$\sigma^2_{\overline{c},p}(n,r) = \overline{c_p(n,r)}^2\left(\frac{\langle c_m(n)\rangle}{\overline{c_p(n,r)}\sqrt{2}} - 1\right). \tag{7.23}$$

Hence the concentration distribution within the plume follows the 2D Gaussian lamellar distribution (7.21), and the rate of scalar dissipation is given by dilution of the maximum concentration $\langle c_m(n)\rangle$ which decays exponentially with pore number n in 3D random media. In general (7.22), (7.23) hold for any macroscopic concentration distribution $l_p(x,y,n)/l(n)$ arising from any injection protocol at $n = 0$ in both heterogeneous or homogeneous media.

8. Conclusions

Three dimensional pore networks are characterized by i) significant topological complexity inherent to all porous media and ii) highly heterogeneous velocity distributions imparted by ubiquitous no-slip conditions at pore walls, which are further compounded by the distribution of pore sizes. The ubiquity of these mechanisms has significant implications for the prediction and understanding of fluid mixing and macroscopic dispersion in 3D random porous media. The interplay of exponential fluid stretching and broad velocity distributions arising from the no-slip condition generates significantly accelerated mixing via the production of highly striated, lamellar concentration distributions.

Conversely, classical conceptual models which are implicitly based upon transport in a two dimensional pore-space impart topological constraints upon streamline dynamics (i.e. forbidding streamline crossing) which limit fluid stretching to grow algebraically with time under steady flow conditions. In 3D, chaotic stretching is generated by the critical points which are typically located at pore junctions in the flow field which impart significant stretching and folding of fluid elements during steady advection.

We study these mechanisms in a model 3D open porous network which is homogeneous at the macroscale, and develop a CTRW model for fluid deformation and pore-scale mixing based upon high-resolution CFD simulation of Stokes flow in the network model. Predictions of this model agree very well with direct numerical simulations. Analytic estimates of the mixing dynamics show that mixing and dilution under steady state conditions is controlled by the mean and variance of the fluid stretching rates (quantified respectively by the Lyapunov exponent λ_∞ and the variance σ^2) and the Péclet number Pe, such that the mean concentration decays exponentially with longitudinal advection in 3D random porous media, whereas mean concentration variance decays algebraically in 2D porous media. Whilst highly idealised, these basic mechanisms are universal to 3D porous media and so these results have significant implications for both modelling and understanding mixing in random media.

The developed stretching CTRW model predicts mixing rates for general fluid stretching properties and transit time distributions. Hence, we anticipate that it may be applicable to quantify mixing in a range of porous materials to decipher the role of network topology and structure upon pore scale mixing and thus upon upscaled dilution and mixing-limited reactions. The proposed framework may be extended to transient transport conditions, relevant for instance for pulse tracer injections, through the integration of longitudinal mixing processes.

MD acknowledges the support of the European Research Council (ERC) through the project MHetScale (contract no. 617511), and TLB acknowledges the support of the ERC project ReactiveFronts, and Agence Nationale de la Recherche project Subsurface Mixing and Reaction.

Appendix A. Nonlinear Shear and Non-Stationarity

The nonlinear shear deformation in $\mathcal{M}$ generates deformation not captured by the linearised deformation tensor $\mathbf{F}_{2\mathrm{D}}$ as reflected by the stretching rates shown in Figure 11(a). Such deformation extends the range of stretching beyond $\rho \in [1/2, 2]$ and also increases the asymmetry of the stretching process, increasing both the variance and mean of the stretching distribution over a couplet to $\sigma^2 \approx 0.128$ $\lambda_\infty \approx 0.124$ respectively.

Furthermore, the stretching process over a couplet under $\mathcal{M}$ is both non-stationary and anti-correlated due to preferential alignment of initially random oriented material elements with the pore boundary as they undergo stretching. This is purely a geometric

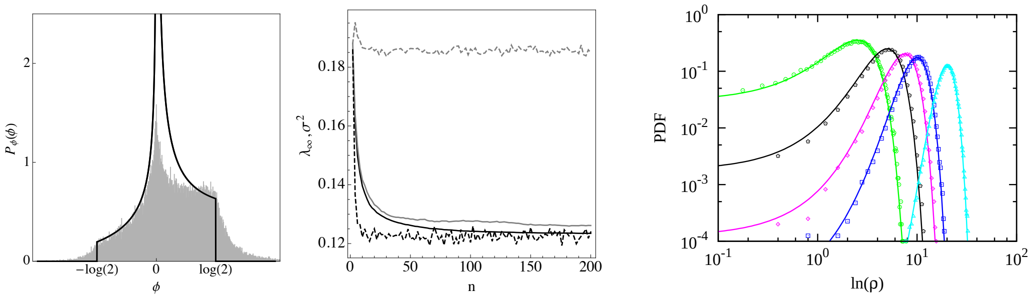

(a) (b) (c)

FIGURE 11. (a) Comparison of the PDFs of logarithmic stretching $P_\phi(\phi)$ over a couplet computed from the nonlinear advective map $\mathcal{M}$ (solid gray) or derived the linearised deformation tensor $\mathbf{F}_{2\text{D}}$ (black line). (b) Evolution of the mean λ_∞ (black, solid) and variance σ^2 (gray, solid) of material deformation with the number of pores n, and convergence of the increment of the mean $\langle\phi_{n+1}\rangle - \langle\phi_n\rangle$ (black, dashed) and variance $\langle(\phi_{n+1} - \langle\phi_{n+1}\rangle)^2\rangle - \langle(\phi_n - \langle\phi_n\rangle)^2\rangle$ (gray, dashed), respectively reflecting anti-correlation and non-stationarity of the adjective map $\mathcal{M}$. (c) Comparison of the lognormal form (4.16) of the PDF of $\ln\rho$ (lines) to the PDFs obtained numerically from the one-step CTRW model (5.2) for (circles) $n = 20$, (pentagons) $n = 40$, (diamonds) n = 60, (squares) $n = 80$, (triangles) $n = 160$.

effect in that highly striated fluid elements must preferentially align tangentially with the pore boundary to allow packing within a finite domain. As the stretching process under $\mathcal{M}$ rapidly converges (after 20 pores) to a stationary process, the increment of the mean $\langle\phi_{n+1}\rangle - \langle\phi_n\rangle$ and variance $\langle(\phi_{n+1} - \langle\phi_{n+1}\rangle)^2\rangle - \langle(\phi_n - \langle\phi_n\rangle)^2\rangle$ quickly converge as per Figure 11(b). Conversely, anti-correlation causes these moments to converge more slowly toward the asymptotic values $\lambda_\infty \approx 0.128$, $\sigma^2 \approx 0.124$. Rather than develop a stochastic model which fully captures non-stationarity and anti-correlation, we approximate this process by using the uncorrelated and stationary one-step stretching CTRW (5.2), where the increment ϕ is from the distribution shown in Figure 11(a) with mean and variance given by these asymptotic values. Figure 11(c) shows that the lognormal form (4.16) parameterized by the asymptotic values of $\lambda_\infty \approx 0.128$, $\sigma^2 \approx 0.124$ compares very well with PDFs of $\ln\rho$ from direct numerical calculation.

Appendix B. Distribution of Transit Times–The Landau Distribution

The PDF $p_n(t)$ of t_n given in (5.1) can be written in Laplace space as

$$p_n^*(\lambda) = \psi^*(\lambda)^n. \tag{B 1}$$

The Pareto distribution (4.18) is a Levy-stable distribution, which means in particular that the long time behavior of $p_n(t)$ is the same as the one of (4.18). The dimensionless Pareto distribution (4.18) is $\psi(\Delta t) = 1/\Delta t^2$, $\Delta t > 1$, and its Laplace transform is then

$$\psi^*(\lambda) = \exp(-\lambda) + \lambda \text{Ei}(-\lambda), \tag{B 2}$$

where $\text{Ei}(x)$ is the exponential integral (Abramowitz & Stegun 1972). For small $\lambda \ll 1$, this expression can be expanded as

$$\psi^*(\lambda) = 1 - \lambda(1-\gamma) + \lambda\ln(\lambda) + \dots. \tag{B 3}$$

Thus we can write $p_n^*(\lambda)$ for small $\lambda \ll 1$ as

$$p_n^*(\lambda) = \exp\left[-\lambda n(\ln n + 1 - \gamma) + \lambda n \ln(\lambda n)\right]. \tag{B 4}$$

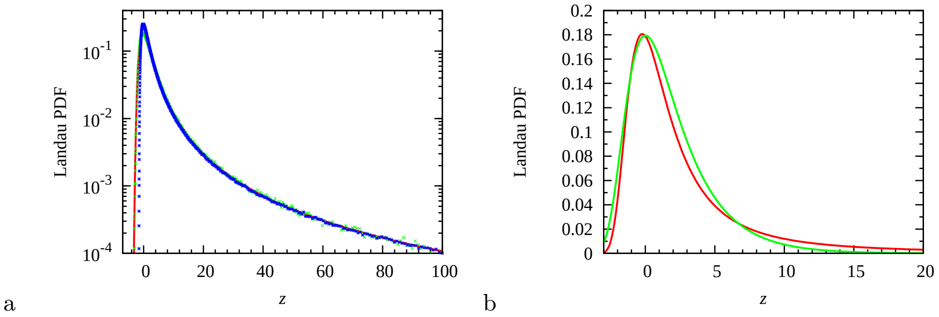

FIGURE 12. Left:c Rescaled and shifted PDF $\hat{p}_n(z)$ for (blue) $n = 10$ and (green) $n = 10^3$ obtained from random walk simulations for 10^6 realizations of the stochastic process t_n. The red line indicates the Landau PDF obtained from numerical inverse Laplace transform of (B 6). Right: Comparison of the (red) Landau PDF $f_1(z)$ defined by (B 6) and (green) the approximation (B 8) by the Moyal distribution.

The inverse Laplace transform of this expression, gives for $p_n(t)$

$$p_n(t) = \frac{1}{n} f_1\left[\frac{t - n(\ln n + 1 - \gamma)}{n}\right], \tag{B 5}$$

where

$$f_1(t) = \int \frac{d\lambda}{2\pi i} \exp\left[\lambda \ln(\lambda)\right] \exp(-\lambda t). \tag{B 6}$$

denotes the Landau distribution (Uchaikin & Zolotarev 1999), which scales as $f_1(t) \approx t^{-2}$ for $t \gg 1$. Expression (B 5) describes the density $p_n(t)$ in the limit of large t or large n. In order to test this approximation, we performed numerical random walk simulations for 10^6 realizations of the random time t_n. The obtained PDF $p_n(t)$ is rescaled as

$$\hat{p}_n(z) = n p_n\left[nz + n(\ln n + 1 - \gamma)\right], \tag{B 7}$$

In the limit $n \to \infty$, we expect $\hat{p}_n(z) \to f_1(z)$. Figure 12 shows $\hat{p}_n(z)$ for $n = 10$ and 10^3 compared to (B 6), which is obtained by numerical inverse Laplace transform. The maximum of (B 6) is assumed at $t_m = -\frac{1}{2}\ln\frac{\pi}{2}$, as illustrated in Figure 12b.

We consider now the average $\langle \ln t_n \rangle$, which is dominated by the bulk of the Landau distribution $p_n(t)$. To this end, we note that the bulk of the Landau distribution $f_1(t)$ can be approximated by the Moyal distribution

$$f_m(x) = \frac{1}{\sqrt{2\pi}} \exp\left[-\frac{1}{2}\left(x + \mathrm{e}^{-x}\right)\right] \qquad \text{as} \qquad f_1(t) = a f_m\left[a(t - b)\right], \tag{B 8}$$

with $a = 0.7413$ and $b = 0.0064$. Thus, we may approximate $p_n(t)$ in terms of $f_m(x)$ as

$$p_n(t) \approx \frac{a}{n} f_m\left(a\left[\frac{t - n(\ln n + 1 - \gamma)}{n} - b\right]\right) \tag{B 9}$$

The mean of $\ln t_n$ is then approximated by

$$\langle \ln t_n \rangle \approx \int\limits_{-\infty}^{\infty} dx \ln\left[n(\ln n + 1 - \gamma) + \frac{n}{a}(\langle x_m \rangle + b) + \frac{nx}{a}\right] f_m(\langle x_m \rangle + x), \tag{B 10}$$

where $\langle x_m \rangle = \ln 2 + \gamma$ is the mean of the Moyal distribution. Thus, we obtain approximately for $\langle \ln t_n \rangle$

$$\langle \ln t_n \rangle \approx \ln \left[\frac{n}{a} \left(\ln 2 + \gamma + b \right) + n \left(\ln n + 1 - \gamma \right) \right] = \ln(\langle t_n \rangle), \tag{B 11}$$

where the mean $\langle t_n \rangle$ of the Moyal distribution (B 9) is given by

$$\langle t_n \rangle \approx \frac{n}{a} \left(\ln 2 + \gamma + b \right) + n \left(\ln n + 1 - \gamma \right). \tag{B 12}$$

We consider now the average over $\sqrt{t_n + Pe\, \rho_n^{-2}}$, which is required to estimated the average mixing scale (7.2). It is also dominated by the bulk of the Landau distribution. As in (B 10), $\left\langle \sqrt{t_n + Pe\, \rho_n^{-2}} \right\rangle$ can be approximated as

$$\int_{-\infty}^{\infty} dx f_m(\langle x_m \rangle + x) \sqrt{\left[n(\ln n + 1 - \gamma) + \frac{n}{a}(\langle x_m \rangle + b) + \frac{nx}{a} \right] + Pe\, \rho_n^{-2}}, \tag{B 13}$$

As above, this expression can be approximated by

$$\left\langle \sqrt{t_n + Pe\, \rho_n^{-2}} \right\rangle \approx \sqrt{\langle t_n \rangle + Pe\, \rho_n^{-2}}. \tag{B 14}$$

REFERENCES

ABRAMOWITZ, M & STEGUN, I. A. 1972 *Handbook of Mathematical Functions*. Dover Publications, New York.

DE ANNA, P., JIMENEZ-MARTINEZ, J., TABUTEAU, H., TURUBAN, R., LE BORGNE, T., DERRIEN, M. & MÉHEUST, Y. 2014 Mixing and reaction kinetics in porous media: An experimental pore scale quantification. *Environ. Sci. Technol.* **48** (508-516).

DE ANNA, P., LE BORGNE, T., DENTZ, M., TARTAKOVSKY, A. M., BOLSTER, D. & DAVY, P. 2013 Flow intermittency, dispersion, and correlated continuous time random walks in porous media. *Phys. Rev. Lett.* **110**, 184502.

BAJER, K. 1994 Hamiltonian formulation of the equations of streamlines in three-dimensional steady flows. *Chaos, Solitons and Fractals* **4** (6), 895–911.

BAJER, K. & MOFFATT, H. K. 1990 On a class of steady confined Stokes flows with chaotic streamlines. *Journal of Fluid Mechanics* **212**, 337–363.

DE BARROS, F., DENTZ, M., KOCH, J. & NOWAK, W. 2012 Flow topology and scalar mixing in spatially heterogeneous flow fields. *Geophys. Res. Lett.* **39**, L08404.

BATTIATO, I., TARTAKOVSKY, D. M., TARTAKOVSKY, A. M. & SCHEIBE, T. 2009 On breakdown of macroscopic models of mixing-controlled heterogeneous reactions in poroous media. *Adv. Water Resour.* **32**, 1664–1673.

BERKOWITZ, B., CORTIS, A., DENTZ, M & SCHER, H. 2006 Modeling non-fickian transport in geological formations as a continuous time random walk. *Rev. Geophys.* **44**, RG2003.

BIJELJIC, BRANKO, MOSTAGHIMI, PEYMAN & BLUNT, MARTIN J. 2011 Signature of non-fickian solute transport in complex heterogeneous porous media. *Phys. Rev. Lett.* **107**, 204502.

BIJELJIC, B., MUGGERIDGE, A. H. & BLUNT, M. J. 2003 Pore-scale modeling of longitudinal dispersion. *Water Resources Research* **40**, W11501.

CHIOGNA, G., HOCHSTETLER, D.L., BELLIN, A., KITANIDIS, P.K. & ROLLE, M. 2012 Mixing, entropy and reactive solute transport. geophysical research letters, 39, doi: 10.1029/2012gl053295. *Geophys. Res. Lett.* **39**.

CHONG, M. S., MONTY, J. P., CHIN, C. & MARUSIC, I. 2012 The topology of skin friction and surface velocity fields in wall-bounded flows. *Journal of Turbulence* **13** (6), 1–10.

DENTZ, MARCO, LE BORGNE, TANGUY, LESTER, DANIEL R. & DE BARROS, FELIPE P. J. 2015 Scaling forms of particle densities for Lévy walks and strong anomalous diffusion. *Phys. Rev. E* **92**, 032128.

DENTZ, M., LEBORGNE, T., ENGLERT, A. & BIJELJIC, B. 2011 Mixing, spreading and reaction in heterogeneous media: A brief review. *J. Cont. Hydrol.* **120-121**, 1–17.

Duplat, J., Innocenti, C. & Villermaux, E. 2010 A nonsequential turbulent mixing process. *Phys. Fluids* **22**, 035104.

Duplat, J. & Villermaux, E. 2008 Mixing by random stirring in confined mixtures. *J. Fluid Mech.* **617**, 51–86.

Erdélyi, A. 1956 *Asymptotic Expansions*. Dover Publications, New York.

Gramling, C. M., Harvey, C. F. & Meigs, L. C. 2002 Reactive transport in porous media: A comparison of model prediction with laboratory visualization. *Environ. Sci. Technol.* **36**, 2508–2514.

Holzner, M., Morales, V. L., Willmann, M. & Dentz, M. 2015 Intermittent lagrangian velocities and accelerations in three-dimensional porous medium flow. *Phys. Rev. E* **92**, 013015.

Jones, Scott W., Thomas, Oran M. & Aref, Hassan 1989 Chaotic advection by laminar flow in a twisted pipe. *Journal of Fluid Mechanics* **209**, 335–357.

Kang, P. K., de Anna, P., Nunes, J. P., Bijeljic, B., Blunt, M. & Juanes, R. 2014 Pore-scale intermittent velocity structure underpinning anomalous transport through 3d porous media. *Geophys. Res. Lett.* **41**, 6184.

Le Borgne, T., Bolster, D., Dentz, M., de Anna, P. & Tartakovsky, A. 2011 Effective pore-scale dispersion upscaling with a correlated continuous time random walk approach. *Water Resour. Res.* **47**, W12538.

Le Borgne, T., Dentz, M. & Villermaux, E. 2013 Stretching, coalescence, and mixing in porous media. *Phys. Rev. Lett.* **110** (20), 204501.

Le Borgne, T., Dentz, M. & Villermaux, E. 2015 The lamellar description of mixing in porous media. *J. Fluid Mech.* **770**, 458–498.

Lester, D. R., Metcalfe, G. & Trefry, M. G. 2013 Is chaotic advection inherent to porous media flow? *Phys. Rev. Lett.* **111**, 174101.

Lester, D. R., Metcalfe, G. & Trefry, M. G. 2014 Anomalous transport and chaotic advection in homogeneous porous media. *Phys. Rev. E* **90**, 063012.

Lester, D. R., Trefry, M. G. & Metcalfe, G. 2016 Chaotic advection at the pore scale: Mechanisms, upscaling and implications for macroscopic transport. *Advances in Water Resources* **in review**.

MacKay, R. S. 1994 Transport in 3D volume-preserving flows. *Journal of Nonlinear Science* **4**, 329–354, 10.1007/BF02430637.

MacKay, Robert S. 2008 A steady mixing flow with non-slip boundaries. In *Chaos, Complexity and Transport* (ed. C. Chandre, X. Leoncini & G. M. Zaslavsky), pp. 55–68. World Scientific.

Metcalfe, G., Speetjens, M.F.M., Lester, D.R. & Clercx, H.J.H. 2012 Beyond passive: Chaotic transport in stirred fluids. In *Advances in Applied Mechanics* (ed. Erik van der Giessen & Hassan Aref), *Advances in Applied Mechanics*, vol. 45, pp. 109 – 188. Elsevier.

Meunier, P. & Villermaux, E. 2010 The diffusive strip method for scalar mixing in two dimensions. *J. Fluid Mech.* **662**, 134–172.

Mezić, I. & Wiggins, S. 1994 On the integrability and perturbations of three-dimensional fluid flows with symmetry. *Journal of Nonlinear Science* **4**, 157–194.

Moroni, M. & Cushman, J.H. 2001 Three-dimensional particle tracking velocimetry studies of the transition from pore dispersion to fickian dispersion for homogeneous porous media. *Water Resour. Res.* **37** (4), 873–884.

Ottino, J. M. 1989 *The Kinematics of Mixing: Stretching, Chaos, and Transport*. Cambridge, United Kingdom: Cambridge University Press.

Ottino, Julio M. & Wiggins, Stephen 2004 Introduction: mixing in microfluidics. *Philosophical Transactions of the Royal Society of London. Series A:Mathematical, Physical and Engineering Sciences* **362** (1818), 923–935.

Ranz, W. E. 1979 Application of a stretch model to mixing, diffusion and reaction in laminar and turbulent flows. *AIChE Journal* **25** (1), 41–47.

Scholz, Christian, Wirner, Frank, Götz, Jan, Rüde, Ulrich, Schröder-Turk, Gerd E., Mecke, Klaus & Bechinger, Clemens 2012 Permeability of porous materials determined from the euler characteristic. *Phys. Rev. Lett.* **109**, 264504.

Siena, M., Riva, M., Hyman, J.D., Winter, C.L. & Guadagnini, A. 2014 Relationship between pore size and velocity probability distributions in stochastically generated porous media. *Phys. Rev. E* **89** (1), 013018.

Surana, A., Grunberg, O. & Haller, G. 2006 Exact theory of three-dimensional flow separation. part 1. steady separation. *Journal of Fluid Mechanics* **564**.

Tartakovsky, A. M., Redden, G., Lichtner, P. C., Scheibe, T. D. & Meakin, P. 2008*a* Mixing-induced precipitation: Experimental study and multiscale numerical analysis. *Water Resour. Res.* **44**, W06S04.

Tartakovsky, A. M., Tartakovsky, D. M. & Meakin, P. 2008*b* Stochastic Langevin model for flow and transport in porous media. *Phys. Rev. Lett.* **101**, 044502.

Tartakovsky, A. M., Tartakovsky, D. M., Scheibe, T. D. & Meakin, P. 2008*c* Hybrid simulations of reaction-diffusion systems in porous media. *SIAM J. Sci. Comput.* **30** (6), 2799–2816.

Tartakovsky, A. M., Tartakovsky, G. D. & Scheibe, T. D. 2009 Effects of incomplete mixing on multicomponent reactive transport. *Adv. Water Resour.* **32**, 1674–1679,.

Uchaikin, V. V. & Zolotarev, M. Z. 1999 *Chance and Stability, Stable Distributions and Their Applications*. Walter de Gruyter.

Villermaux, E. 2012 Mixing by porous media. *C. R. Mécanique* **340**, 933–943.

Villermaux, E. & Duplat, J. 2003 Mixing as an aggregation process. *Phys. Rev. Lett.* **91**, 18.

Vogel, H. J. 2002 Topological characterization of porous media. In *Morphology of Condensed Matter* (ed. Klaus Mecke & Dietrich Stoyan), *Lecture Notes in Physics*, vol. 600, pp. 75–92. Springer Berlin Heidelberg.

Wiggins, S. 2010 Coherent structures and chaotic advection in three dimensions. *Journal of Fluid Mechanics* **654**, 1–4.

de Winkel, E.M. & Bakker, P.G. 1988 *On the Topology of Three-dimensional Viscous Flow Structures Near a Plane Wall: A Classification of Hyperbolic and Non-hyperbolic Singularities on the Wall*. Delft University of Technology, Faculty of Aerospace Engineering.